bioRxiv preprint doi: https://doi.org/10.64898/2026.04.21.720027; this version posted April 24, 2026. The copyright holder for this preprint (which was not certified by peer review) is the author/funder, who has granted bioRxiv a license to display the preprint in perpetuity. It is made available under a CC-BY-NC-ND 4.0 International license.

A Patient-derived Organoid Platform for Uterine Carcinosarcoma that Emulates Disease Characteristics

Santhilal Subhash[1,2,9], Marie-Thérèse Bammert[1,9], Brian Yueh[1,9], Kadir A. Ozler[1], Timothy Chu[3], Melissa Kramer[1], Pascal Belleau[1], Astrid Deschênes[1], Onur Eskiocak[1,4], Charlie Chung[1,4], Ali Oku[3], Mali Barbi[1,5], Aybuke Alici[1], Megan Gorman[6], Arielle Katcher[6], Aaron Nizam[6], Ariel Kredentser[6], Divya Bhana[6], Jonathan Werner[1], Nicolas Robine[3], Marina Frimer[6,8], Gary L. Goldberg[1,6,8], Semir Beyaz[1,*]

[1] Cold Spring Harbor Laboratory, Cold Spring Harbor, NY, USA

[2] Department of Biosciences and Bioengineering, Indian Institute of Technology Jammu, Jammu, India

[3] New York Genome Center, New York, NY, USA

[4] Graduate Program in Genetics, Stony Brook University, Stony Brook, NY, USA

[5] Northwell Health Cancer Institute, New Hyde Park, NY, USA

[6] Division of Gynecologic Oncology, Department of Obstetrics and Gynecology, Northwell Health, Zucker School of Medicine at Hofstra/Northwell, New Hyde Park, NY, USA

[7]Department of Pathology, Renaissance School of Medicine, Stony Brook University, Stony Brook, NY, USA.

[8] Feinstein Institutes for Medical Research, Manhasset, NY, USA

[9] These authors contributed equally

*Correspondence: beyaz@cshl.edu

bioRxiv preprint doi: https://doi.org/10.64898/2026.04.21.720027; this version posted April 24, 2026. The copyright holder for this preprint (which was not certified by peer review) is the author/funder, who has granted bioRxiv a license to display the preprint in perpetuity. It is made available under a CC-BY-NC-ND 4.0 International license.

Abstract

Uterine carcinosarcoma (UCS) is a rare but highly lethal endometrial malignancy characterized by early dissemination, marked lineage plasticity, and limited therapeutic options. Although genomic studies have established UCS as a copy-number-high, carcinoma-like tumor with strong epithelial-mesenchymal transition (EMT) features, mechanistic and translational progress has been hindered by the lack of physiologically relevant patient-derived models, particularly models representing patients from African ancestry who are disproportionately affected by UCS. Here, we establish an ancestrally diverse cohort of UCS patient-derived organoids (PDOs) with matched normal endometrial PDOs that preserve the histological, genomic and transcriptional features of the tumors from which they were derived. Across the cohort, UCS PDOs retain somatic mutations, copy number alterations and recapitulate biphasic epithelial and mesenchymal cell states at single-cell resolution, and model dynamic transitions along an epithelial-to-mesenchymal continuum. Integrated bulk and single-cell analyses identify mesenchymal, proliferative, and metabolic transcriptional programs in UCS, with prominent enrichment of CREB-family motifs. Functionally, UCS PDOs reproduce heterogeneous responses to carboplatin and paclitaxel, reveal sensitivity to CREB inhibition, and suggest a potential cooperative vulnerability to combined FGFR and YAP pathway inhibition. Together, these data establish a genomically faithful and ancestrally inclusive UCS PDOs platform for studying tumor plasticity, lineage-state regulation, and therapy response in an understudied and clinically aggressive gynecologic cancer.

bioRxiv preprint doi: https://doi.org/10.64898/2026.04.21.720027; this version posted April 24, 2026. The copyright holder for this preprint (which was not certified by peer review) is the author/funder, who has granted bioRxiv a license to display the preprint in perpetuity. It is made available under a CC-BY-NC-ND 4.0 International license.

MAIN

Introduction

Uterine carcinosarcoma (UCS) is an aggressive subtype of endometrial cancer defined by its biphasic architecture, comprising malignant epithelial and sarcoma-like components[1–3]. Although UCS represents a minority of endometrial cancers, it accounts for a disproportionate number of disease-related deaths due to rapid progression, early dissemination, and high recurrence rate. Standard-of-care treatment consists of surgery followed by platinum- and taxane-based chemotherapy[1,4–6]; however, therapeutic responses are frequently transient and relapse is common. Clinical management is largely extrapolated from other high-grade endometrial or ovarian cancers, yet survival outcomes remain poor and there is no consensus on effective UCS-specific regimens, highlighting a significant unmet medical need[7–9].

Despite its clinical aggressiveness, progress in understanding UCS biology has been limited by the lack of physiologically relevant models that capture its biphasic lineage composition and dynamic cell-state transitions. This gap is further compounded by the underrepresentation of diverse patient populations in current preclinical and translational studies[10,11], despite known disparities in UCS incidence, severity, and outcomes across ancestry, age, and metabolic context[12,13,14]. As a result, current models fail to reflect the full biological and clinical heterogeneity of UCS, restricting mechanistic insight and the identification of actionable therapeutic vulnerabilities. To address these challenges, there is a need for model systems that not only preserve the genomic and transcriptional architecture of primary tumors but also recapitulate their cellular heterogeneity, lineage plasticity, and treatment responses. In particular, models that demonstrate concordance with primary tumors at the level of mutational landscape, copy-number alterations, and cell-state-specific transcriptional programs are essential to enable functional interrogation and therapeutic testing.

Conventional two-dimensional cell lines fail to recapitulate the biphasic organization, intercellular signaling networks, and lineage heterogeneity that define primary tumors, while prolonged *in vitro* cultivation often selects for dominant clones, erasing patient-specific plastic states[15,16]. *In vivo* models, while informative, are constrained by interspecies anatomical and reproductive cyclic differences between rodents and humans, which limit full physiological translatability and fail to

bioRxiv preprint doi: https://doi.org/10.64898/2026.04.21.720027; this version posted April 24, 2026. The copyright holder for this preprint (which was not certified by peer review) is the author/funder, who has granted bioRxiv a license to display the preprint in perpetuity. It is made available under a CC-BY-NC-ND 4.0 International license.

adequately capture the complexity and diversity of human endometrial tumors[17,18]. Patient-derived organoids (PDOs) provide a powerful framework to overcome these barriers by preserving three-dimensional architecture, tumor-intrinsic heterogeneity, and patient-specific molecular features while enabling functional interrogation of therapeutic responses in a controlled yet physiologically relevant context[19]. However, robust and inclusive organoid models of UCS that integrate genomic fidelity, lineage-resolved transcriptomics, and systematic chemotherapy modeling have not been comprehensively established[20–22].

Here, we establish an ancestrally diverse cohort of UCS PDOs and matched normal tissues that faithfully recapitulate the genetic, transcriptional, and cellular features of primary tumors. Through integrated whole-genome sequencing, bulk and single-cell transcriptomics, and functional perturbation assays, we demonstrate high concordance between UCS PDOs and their tumors of origin, including preservation of biphasic epithelial and mesenchymal lineage states and inter-patient heterogeneity. We further show that these models capture key signaling dependencies and chemotherapeutic responses, enabling the identification of state-dependent vulnerabilities and providing a scalable platform for mechanistic studies. Together, this work closes a critical gap in UCS research by establishing a genomically and transcriptionally faithful, ancestrally inclusive PDO model system that enables the study of tumor plasticity, cell-state interactions, and therapeutic response, thereby advancing both biological understanding and translational opportunities in this lethal disease.

Results

Genomically defined and ancestrally inclusive UCS cohort enables PDO modeling

To establish a clinically relevant UCS model resource, we collected 25 UCS tumor specimens (23 primary tumors and 2 metastases) together with matched normal tissue when available and processed them for PDO derivation and molecular profiling (**Figure 1A**). Since UCS disproportionately affects women of African American (AFR) ancestry[23,24] and prior The Cancer Genome Atlas (TCGA)-UCS studies included only 16% (9/57) AFR patients[25], our cohort was intentionally enriched for diversity, comprising 60% (15/25) AFR women to address this health disparity. Patients were stratified by BMI and age (**Figure 1B**), and self-reported ethnicity. WGS was performed on all 25 specimens to define somatic and germline alterations (**Figure 1C**).

bioRxiv preprint doi: https://doi.org/10.64898/2026.04.21.720027; this version posted April 24, 2026. The copyright holder for this preprint (which was not certified by peer review) is the author/funder, who has granted bioRxiv a license to display the preprint in perpetuity. It is made available under a CC-BY-NC-ND 4.0 International license.

Genetic ancestry was determined from germline single nucleotide variants by projecting samples onto reference populations using ADMIXTURE[26] inference. The predominant (max) ancestry for each specimen was defined as the ancestry component with the highest proportional contribution. Consistent with TCGA-UCS data[25], *TP53* mutations were highly prevalent and detected in 21 of 25 tumors, underscoring the serous-like, copy-number high molecular architecture characteristic of UCS[27]. Additional mutations, including *ARID1A*, *PTEN*, *KEAP1*, *PAX8*, and *ASPSCR1*, varied across patients, reflecting substantial inter-tumoral heterogeneity. MANTIS[28] analysis further identified one case (CS-014T) as microsatellite instability-high (MSI-H) with elevated tumor mutational burden (TMB), highlighting the presence of distinct molecular subsets within the cohort (**Figure 1C**).

Collectively, this ancestrally enriched and genomically characterized UCS cohort provides a valuable resource that captures both canonical *TP53*-driven biology and patient-specific heterogeneity, establishing a robust foundation for organoid-based studies of tumor plasticity, therapeutic vulnerability, and drug response.

FGFR genomic alterations inform FGF-dependent establishment and long-term expansion of UCS PDOs

We next asked whether recurrent growth factor signaling alterations in UCS could help guide culture conditions for robust PDO establishment. UCS PDOs were established and expanded according to previously published protocols[29–31], followed by comprehensive genomic, transcriptomic, and histologic profiling to interrogate UCS pathophysiology and identify candidate molecular targets. Analysis of the TCGA-UCS cohort (n = 56) revealed recurrent alterations in growth factor receptor genes, with the most prominent events involving *FGFR3*, *FGFR1*, and *FGFR2*, along with less frequent alterations in *PDGFRA*, *PDGFRB*, and *IGF1R* (**Figure 2A**). Because these events include amplification, mutation, and deletion, our data suggest a pathway-level dysregulation rather than a single recurrent hotspot event.

To test whether genomic alteration translated into transcriptional output, we compared copy-number and RNA expression measurements for *FGFR1* and *FGFR3* in our cohort (n = 25, red) and in TCGA-UCS[25] (n = 56, blue). In both, increased copy number was associated with higher

bioRxiv preprint doi: https://doi.org/10.64898/2026.04.21.720027; this version posted April 24, 2026. The copyright holder for this preprint (which was not certified by peer review) is the author/funder, who has granted bioRxiv a license to display the preprint in perpetuity. It is made available under a CC-BY-NC-ND 4.0 International license.

transcript abundance, although the effect sizes were modest, which is expected for pathway components influenced by both dosage and cell-state context (**Figure 2B**).

Based on these observations, we hypothesized that FGF signaling may provide critical growth support for UCS cells *in vitro*. We therefore systematically tested individual FGF ligands and combinations during PDO establishment. Among tested conditions, FGF1, FGF4 and FGF9, ligands known to signal predominantly through FGFR1 and FGFR3[32], robustly supported PDO formation either individually or in combination (**Figure S2A-B**). Incorporation of FGF1 and FGF4 into an optimized culture system resulted in successful establishment of UCS PDOs with an overall efficiency of approximately 85% across donors (**Figure S2C**).

Brightfield imaging demonstrated stable three-dimensional architecture of UCS PDOs, which were morphologically distinct from matched normal endometrial PDOs derived from the same patients (**Figure 2C** and **Figure S2D**). Importantly, we have established UCS PDO models with a long term expansion potential for up to 24 months. (**Figure 2D** and **Figure S2E**). Quantification further showed an increase in PDO yield between early and later culture time points, indicating that PDO-forming cells remain proliferative and undergo expansion over time in culture (**Figure S2F**). A subset of these UCS PDOs were expanded for the Human Cancer Models Initiative for distribution with the scientific community[33].

To evaluate whether tumor-intrinsic genomic features were preserved *in vitro*, we performed matched whole exome sequencing (WES) and bulk RNA-seq on three established UCS PDOs. We integrated UCS PDO transcriptomic profiles with their corresponding copy-number landscapes and conducted the same copy-number-expression correlation analysis as in primary tumors. Consistent with patient tissue and TCGA-UCS samples, *FGFR1* and *FGFR3* copy-number gains in UCS PDOs were associated with increased transcript abundance (**Figure 2E**).

Collectively, these findings demonstrate that FGFR pathway is altered in UCS and incorporating FGFs support the robust establishment and long-term expansion of ancestrally diverse UCS PDO models.

bioRxiv preprint doi: https://doi.org/10.64898/2026.04.21.720027; this version posted April 24, 2026. The copyright holder for this preprint (which was not certified by peer review) is the author/funder, who has granted bioRxiv a license to display the preprint in perpetuity. It is made available under a CC-BY-NC-ND 4.0 International license.

UCS PDOs recapitulate histopathologic and phenotypic features of primary tumors

To assess whether UCS PDOs preserve histopathological features of the parental tumors, we performed comparative hematoxylin and eosin (H&E) staining and immunohistochemical (IHC) analyses on matched primary tissues and PDOs. Primary UCS specimens displayed characteristic biphasic morphology, with malignant epithelial glandular structures intermingled with atypical mesenchymal stroma (**Figure 3A**). High-grade nuclear atypia and stromal expansion were evident across cases (**Figure 3A**, highlighted by asterisk and arrows).

Immunohistochemical staining of primary UCS tumors confirmed epithelial differentiation by E-cadherin (CDH1) positivity and epithelial membrane antigen (EMA) expression, while diffuse p53 staining was observed, consistent with the high frequency of *TP53* alterations identified genomically. Robust Ki67 labeling further indicated high proliferative activity within both epithelial and stromal compartments (**Figure 3B**).

Histological examination of UCS PDOs demonstrated preservation of malignant architectural features[34], including high-grade nuclear atypia and regions of central necrosis (**Figure 3C** and **Figure S3A-D**). UCS PDOs displayed complex three-dimensional organization, and in some regions, extracellular matrix-like structures were observed, suggestive of stromal-like differentiation (**Figure 3C**, right image, highlighted by arrow). These findings indicate that PDOs maintain structural features reminiscent of the biphasic nature of UCS.

Immunostaining of UCS PDO sections revealed cellular marker expression patterns comparable to the corresponding primary tumors. CDH1 confirmed epithelial components within PDOs, EMA marked epithelial differentiation, diffuse p53 expression reflected retention of *TP53*-altered tumor identity, and Ki67 staining demonstrated sustained proliferative capacity *in vitro* (**Figure 3D** and **Figure S3A-D**). Together, these data demonstrate that UCS PDOs preserve key histopathological characteristics of the parental tumors, supporting their suitability as clinically-relevant models.

UCS PDOs preserve the genomic landscape and copy-number architecture of primary tumors

bioRxiv preprint doi: https://doi.org/10.64898/2026.04.21.720027; this version posted April 24, 2026. The copyright holder for this preprint (which was not certified by peer review) is the author/funder, who has granted bioRxiv a license to display the preprint in perpetuity. It is made available under a CC-BY-NC-ND 4.0 International license.

To investigate in genomic concordance between primary tumors and matched UCS PDOs, we performed multi-layered genomic profiling across sequencing platforms. Targeted panel sequencing of 49 recurrent cancer-associated genes was conducted on 25 tumor tissues (23 primary tumors and 2 metastases) and matched UCS PDO lines (**Figure 4A** and **Figure S4A**). Across samples, recurrent alterations were detected in canonical carcinosarcoma-associated genes, including *TP53*, *KRAS*, *PIK3CA*, *ARID1A*, and *TGFB2*, consistent with prior genomic studies[10,25,35,36]. Importantly, matched PDOs retained the vast majority of somatic mutations detected in their parental tumors (**Figure 4A** and **Figure S4A**). For example, a frameshift deletion in *ARID1A* was detected in both primary tumors and matched UCS PDOs (**Figure 4A**).

To quantify overlap between primary tumors and UCS PDOs, we compared single nucleotide polymorphisms (SNPs) identified across matched samples. Of the detected variants, 862 SNPs were shared between primary tissues and UCS PDOs, whereas 36 were exclusive to primary tumors and 30 were unique to UCS PDOs (**Figure 4B**).

To complement targeted genomic profiling, we performed whole-exome sequencing (WES) on three matched primary UCS tumor-PDO pairs (eight total lines including independent passages) to evaluate broader genomic concordance (**Figure 4C-D** and **Figure S4B-C**). Somatic mutation spectra were highly similar between matched pairs, and hierarchical clustering based on variant profiles grouped PDOs with their respective parental tumors. Importantly, analysis of copy-number alterations demonstrated concordance in both amplification and deletion events across matched samples, with high pairwise correlation coefficients (**Figure 4C-D**).

Given that UCS is characterized by widespread copy-number instability[25], we next performed Short Multiply Aggregated Sequence Homologies (SMASH) sequencing to generate genome-wide copy-number profiles. SMASH analysis confirmed that UCS PDOs maintained large-scale chromosomal amplifications and deletions observed in the corresponding primary tumors (**Figure 4E**). Moreover, copy-number landscapes were stable across serial passages, indicating genomic stability during long-term *in vitro* culture. Correlation analyses of amplification and deletion profiles further demonstrated that UCS PDOs clustered with their matched primary tumors rather than with unrelated samples (**Figure 4F**).

bioRxiv preprint doi: https://doi.org/10.64898/2026.04.21.720027; this version posted April 24, 2026. The copyright holder for this preprint (which was not certified by peer review) is the author/funder, who has granted bioRxiv a license to display the preprint in perpetuity. It is made available under a CC-BY-NC-ND 4.0 International license.

Collectively, these multi-platform genomic analyses demonstrate that UCS PDOs faithfully preserve the mutational landscape and copy-number architecture of their parental tumors, supporting their use as a robust and genomically stable model.

Single-cell transcriptomics reveals cellular heterogeneity and epithelial-mesenchymal plasticity in UCS PDOs

To assess whether UCS PDOs preserve the cellular heterogeneity and lineage complexity of primary tumors, we performed single-cell RNA-seq on four independent UCS PDO lines (CS-007TO, CS-009TO, CS-013TO, and CS-014TO). UMAP embedding revealed distinct donor-specific clustering, reflecting inter-patient transcriptional heterogeneity (**Figure 5A**). Within each UCS patient, cells segregated into carcinoma-like and sarcoma-like compartments, with further subdivision into epithelial basal, glandular, and luminal states, as well as endothelial-like, fibroblast-like, stromal-like, and muscle-like mesenchymal populations. Additional stem-associated clusters, including mesenchymal stem cell (MSC)-like and cancer stem cell (CSC)-like populations, were identified. The relative abundance of these cell states varied markedly across donors (**Figure 5A, lower panel**). Certain cell populations appeared selectively enriched in individual PDOs. For example, fibroblast-like cells were predominantly observed in CS-007TO, whereas CS-009TO displayed an expanded epithelial luminal compartment (**Figure 5A, lower panel**). Donor CS-014TO exhibited a distinct EMT-enriched subpopulation, while MSC-like states were present across donors, albeit with heterogeneous transcriptional signatures (**Figure 5A, lower panel**). These findings indicate that UCS PDOs capture both epithelial and mesenchymal lineages and reflect patient-specific cellular architecture.

To determine whether UCS PDOs maintain transcriptional similarity to primary tumors, we compared cell type-defining gene expression signatures between PDOs and matched tissues. Correlation analyses demonstrated concordance between UCS PDOs and primary tumor transcriptomes across donors ($R = 0.59$-0.94; **Figure 5B**), supporting preservation of tumor-intrinsic transcriptional programs.

We next analyzed transcriptional dynamics within UCS PDOs. RNA velocity analysis in donor CS-014TO revealed directional flow from epithelial basal and glandular populations toward EMT

bioRxiv preprint doi: https://doi.org/10.64898/2026.04.21.720027; this version posted April 24, 2026. The copyright holder for this preprint (which was not certified by peer review) is the author/funder, who has granted bioRxiv a license to display the preprint in perpetuity. It is made available under a CC-BY-NC-ND 4.0 International license.

and MSC-like states (**Figure 5C**). Pseudotime analysis further resolved cells along an early epithelial, transitional, and late mesenchymal continuum (**Figure 5D**). Latent time modeling confirmed a continuous trajectory, with gene-specific splicing kinetics indicating temporal activation of EMT-associated programs (**Figure 5E**). For example, canonical epithelial markers (e.g., *MUC1*) were enriched in early epithelial states, whereas EMT regulators (e.g., *SNAI2*) peaked during transition, and mesenchymal markers (e.g., *SLPI*) were upregulated at later stages. Importantly, comparable trajectory architectures were observed across additional UCS PDOs (CS-007TO, CS-009TO, and CS-013TO) (**Figure S5C**). In each donor, RNA velocity streams indicated directional progression from epithelial or stem-associated states toward mesenchymal-like compartments, although the dominant originating populations varied between patients (**Figure S5C**).

Collectively, these single-cell analyses demonstrate that UCS PDOs recapitulate patient-specific cellular heterogeneity while preserving dynamic epithelial-mesenchymal state transitions.

Integrated transcriptomic profiling identifies CREB-associated transcriptional programs in UCS PDOs

To define transcriptional programs in UCS PDOs, we performed bulk RNA-seq on eight UCS PDO lines and nine normal or matched endometrial biopsy-derived PDOs. Principal component analysis demonstrated segregation between UCS and normal samples (**Figure S6A**), confirming distinct transcriptomic identities. ADMIXTURE[37]-based ancestry inference from bulk RNA-seq further validated that the majority of sequenced samples were of African ancestry (**Figure S6B**).

Differential expression analysis identified 2,158 significantly deregulated genes in UCS PDOs relative to normal PDO controls (FDR < 0.05), including 1,336 upregulated and 822 downregulated transcripts (**Figure 6A**). Among the most significantly upregulated genes were proliferation- and EMT-associated transcripts (e.g., *KIF5C*, *S100A9*, *SIX1*, *IGF2*), whereas downregulated genes included epithelial-lineage regulators and differentiation-associated transcripts. In addition to protein-coding genes, multiple long non-coding RNAs (lncRNAs) were significantly deregulated, indicating coordinated remodeling of both coding and non-coding transcriptional networks.

bioRxiv preprint doi: https://doi.org/10.64898/2026.04.21.720027; this version posted April 24, 2026. The copyright holder for this preprint (which was not certified by peer review) is the author/funder, who has granted bioRxiv a license to display the preprint in perpetuity. It is made available under a CC-BY-NC-ND 4.0 International license.

Heatmap analysis of lineage-associated gene signatures demonstrated downregulation of canonical epithelial markers (e.g., *EPCAM*, *MUC1*, *CDH1*) and immune-associated genes in UCS PDOs, alongside robust upregulation of mesenchymal and EMT-associated genes (e.g., *VIM*, *FN1*, *SPARC*, *ZEB1*, *SNAI2*) (**Figure 6B**). These bulk-level changes are consistent with the epithelial-mesenchymal plasticity observed at single-cell resolution. Gene set enrichment analysis further revealed significant enrichment of Hallmark pathways associated with EMT, myogenesis, E2F targets, G2/M checkpoint, mTORC1 signaling, glycolysis, and inflammatory signaling (**Figure 6C**), indicating coordinated activation of proliferative and mesenchymal programs. Metabolic reprogramming was also evident, with deregulation of lipid and fatty acid metabolism genes including *CPT1C*, *APOE*, and *APOL1* (**Figure S6E**).

To identify transcription factor associations, we performed promoter motif enrichment analysis on differentially expressed protein-coding genes. Promoters of upregulated genes were significantly enriched for CREB-family binding motifs, including CREB1, CREB3, CREB5, and CREM (**Figure 6D**), implicating CREB-dependent transcriptional activation in UCS. Consistent with this, motif analysis of deregulated lncRNAs revealed enrichment of CREB binding motifs among downregulated lncRNA promoters (**Figure S6F**), suggesting context-dependent regulatory effects across coding and non-coding transcriptional programs.

Collectively, integrated bulk transcriptomic analyses reveal that UCS PDOs are defined by mesenchymal activation, metabolic remodeling, and enrichment of CREB-associated transcriptional programs, nominating CREB signaling as a potential regulatory axis underlying UCS plasticity.

UCS PDOs model heterogeneous drug response and nominate candidate therapeutics

Having established genomically and phenotypically faithful UCS PDOs, we next evaluated their utility as a platform for therapeutic interrogation. As a benchmark, we performed standard-of-care drug screening using Carboplatin (CPT) and Paclitaxel (PTX) alone and in combination, the backbone of treatment for aggressive gynecologic malignancies[38,39]. PTX induced cytotoxicity across most UCS PDO lines, whereas CPT exhibited more variable and donor-dependent effects (**Figure S7A-B**). Combination CPT-PTX treatment resulted in enhanced cytotoxicity in UCS

bioRxiv preprint doi: https://doi.org/10.64898/2026.04.21.720027; this version posted April 24, 2026. The copyright holder for this preprint (which was not certified by peer review) is the author/funder, who has granted bioRxiv a license to display the preprint in perpetuity. It is made available under a CC-BY-NC-ND 4.0 International license.

PDOs compared to single agents in several UCS PDOs (**Figure 7A-B**), consistent with combinatorial efficacy observed in high-grade serous ovarian cancer[6,38,40] and supporting the translational relevance of PDO-based drug testing. These results demonstrate that UCS PDOs recapitulate heterogeneous chemotherapy responses and provide a suitable system to model inter-patient variability in treatment sensitivity.

Building on the transcriptional analyses identifying CREB-family motif enrichment and mesenchymal activation in UCS PDOs, we next investigated whether CREB signaling represents a functional dependency. Pharmacologic inhibition of CREB (666-15) led to a dose-dependent reduction in PDO viability, whereas inhibition of the CREB co-activator CBP/p300 (A-485) exerted comparatively modest effects (**Figure 7C**), indicating that CREB is critical to UCS PDO survival.

Given the recurrent FGFR alterations observed in earlier analyses (**Figure 2A, C, E**), we further examined pathway-directed targeting of FGFR signaling (Futibatinib) and YAP activity (Verteporfin) (**Figure 7D** and **Figure S7C**). Both agents failed to strongly reduce PDO viability as single treatments, but combined inhibition of FGFR and YAP signaling produced cytotoxic effects in UCS PDOs (**Figure 7D** and **Figure S7C**), suggesting cooperative signaling dependencies between FGFR and YAP pathways.

Together, these data show that UCS PDOs exhibit heterogeneous responses to chemotherapy and targeted inhibitors and enable functional assessment of candidate pathway dependencies.

Discussion

The ability to model human disease in systems that retain its defining biological features remains a fundamental challenge in biomedical research. This is particularly critical for malignancies in which cellular identity is not fixed but dynamically regulated through transcriptional and genomic plasticity programs. UCS represents an extreme example of such complexity, yet current models do not adequately capture its biphasic architecture and underlying cell-state dynamics. Here, we establish PDOs intentionally including diverse patient backgrounds that preserve both the genomic landscape and transcriptional heterogeneity of primary UCS tumors. Our UCS PDO models offer

bioRxiv preprint doi: https://doi.org/10.64898/2026.04.21.720027; this version posted April 24, 2026. The copyright holder for this preprint (which was not certified by peer review) is the author/funder, who has granted bioRxiv a license to display the preprint in perpetuity. It is made available under a CC-BY-NC-ND 4.0 International license.

a physiologically relevant framework to interrogate disease mechanisms including cellular plasticity and therapeutic response.

Prior landmark studies established that UCS is a metaplastic carcinoma with extensive copy-number alterations, frequent *TP53* mutations and EMT transcriptional signature[10,25]. Our data demonstrate that UCS PDOs preserve these genomic properties across independent platforms. The relatively high fraction of shared variants and the strong similarity of amplification and deletion profiles indicate that the dominnat tumor genome is maintained *in vitro*, even though limited unique variants suggest that some subclonal representation or culture-related selection is still possible. Our UCS models balance between the fidelity and manageable simplification of the *in vitro* culture conditions.

Single-cell analyses resolved epithelial, stem-like, and mesenchymal populations that were arranged along continuous transcriptional trajectories. Directional RNA velocity and pseudotime analyses consistently indicated transitions from epithelial toward mesenchymal-like states across independent PDO lines, although the dominant originating populations varied between donors. These observations are compatible with a model in which phenotypic diversification in UCS and other tumors arises predominantly from transcriptional state plasticity layered upon a stable genomic backbone[25,41,42].

At the transcriptional level, UCS PDOs exhibited coordinated changes in mesenchymal, proliferative, and metabolic gene programs. The concurrent deregulation of protein-coding transcripts and long non-coding RNAs suggests broader transcriptional remodeling beyond individual pathways, consistent with emerging roles of non-coding RNAs in chromatin organization and EMT regulation[43–45]. Promoter motif analysis identified enrichment of CREB-family binding motifs, and pharmacologic CREB inhibition reduced PDO viability. CREB signaling has been previously linked to proliferation, stress adaptation, and transcriptional plasticity, and is also known to regulate non-coding RNA expression[46–50]. Together, these findings link CREB-associated transcriptional programs to cellular fitness in UCS, while further work will be required to determine whether CREB directly regulates cell state transitions or acts downstream of other signaling inputs.

bioRxiv preprint doi: https://doi.org/10.64898/2026.04.21.720027; this version posted April 24, 2026. The copyright holder for this preprint (which was not certified by peer review) is the author/funder, who has granted bioRxiv a license to display the preprint in perpetuity. It is made available under a CC-BY-NC-ND 4.0 International license.

Recurrent *FGFR* alterations were associated with increased transcript abundance and supported FGF-dependent PDO growth, and combined FGFR and YAP inhibition reduced viability. The observation aligns with findings in which growth factor signaling and mechanotransduction converge to reinforce EMT and stemness programs through shared transcriptional regulators[51]. Additionally, *FGFR1* activating mutations and amplifications have been reported across multiple cancer types and are known to promote tumor cell proliferation and survival, frequently correlating with adverse clinical outcomes[52,53]. Notably, prior preclinical and clinical observations in endometrial cancer, including UCS, have suggested that FGFR pathway inhibition (e.g., with pazopanib) may reduce tumor burden[54,55]. UCS may therefore represent a signaling-integrated ecosystem in which extracellular inputs continuously reinforce transcriptional identity and plasticity. However, the extent to which these signals and pathways converge on shared transcriptional regulators remains to be defined.

While these findings establish PDOs as a robust platform to model UCS-intrinsic transcriptional plasticity, they do not fully recapitulate the multicellular complexity of the tumor microenvironment. In particular, stromal, immune, and vascular compartments, known to critically shape epithelial cell states and therapeutic response[56–58], are not represented in the current system. Recently, we established an autologous co-culture platform using high-grade endometrial cancer PDOs and matched immune cells from the same patients for modeling epithelial-immune interactions and testing the safety and efficacy of immunotherapy drugs *in vitro*[59]. Building on these approaches, future studies should integrate UCS PDOs into more complex co-culture or multi-compartment systems to dissect how extrinsic signals reinforce or constrain transcriptional plasticity and therapy response.

Collectively, we have established a genomically benchmarked, ancestrally enriched, lineage-resolved PDO platform for interrogating the plasticity and therapeutic vulnerability in UCS, a rare and understudied malignancy with significant unmet need.

bioRxiv preprint doi: https://doi.org/10.64898/2026.04.21.720027; this version posted April 24, 2026. The copyright holder for this preprint (which was not certified by peer review) is the author/funder, who has granted bioRxiv a license to display the preprint in perpetuity. It is made available under a CC-BY-NC-ND 4.0 International license.

Methods

Ethical approval

Fresh tumor and normal endometrial tissue specimens were obtained from patients undergoing hysterectomy for UCS from Northwell Health LIJ Medical Center. Institutional Review Board approval was obtained (study IRB #18-0897), and all patients provided informed consent prior to specimen collection.

Endometrial tissue processing and PDOs generation

Isolation of endometrial cells and cultivation of PDOs was performed according to Katcher et al.[29]. In brief, tissue was washed with cold 1X PBS and minced into small (~0.25 cm) fragments, before being transferred to 5 ml of RPMI media (Sigma Aldrich, #R8758) containing 1 mg/mL Collagenase (Sigma Aldrich, #C9407) and 10 µM Y-27632 dihydrochloride (Tocris, #1254). Tissue suspension was transferred to a rotating incubator (speed: 30 rpm, 37 °C) for 60-120 min depending on successful tissue dissociation. Supernatant was transferred and centrifuged at 300 g for 5 min at room temperature (RT). Supernatant was discarded and the pellet was resuspended in 3 mL of TrpLE Express Enzyme (1X, no phenol red, Thermo Fisher Scientific, #12604103) with 10 µM Y-27632 dihydrochloride followed by an incubation of 10-20 min at 37 °C with regular mixing. To stop the reacting 3 mL of ADMEM/F12 (Life Technologies, #312634028) was added and the cell suspension centrifuged at 300 g for 5 min at RT. Cells were embedded in a 70:30 mixture of Matrigel matrix (Corning, #356231): PDO media and seeded in 50 µL domes. After polymerization, normal or tumor endometrial PDO media was added. Media exchange was performed every 3-4 days.

Passaging of endometrial PDOs

Growth was monitored and PDOs passaged every 7-14 days. Therefore, PDOs were collected by removing Matrigel using Cell Recovery Solution (Corning, #354253). After 30 min at 4 °C, PDO suspension was centrifuged at 300 g for 5 min at 4 °C. Supernatant was discarded and PDOs resuspended in 3 mL of TrpLE Express Enzyme, followed by an incubation for 5-15 min at 37 °C. 3 mL of ADMEM/F12 was added and cells centrifuged at 300 g for 5 min at 4 °C, before being seeded again in 70:30 Matrigel:PDO media mixture. Commonly, PDOs were passaged in a 1:2 ratio.

bioRxiv preprint doi: https://doi.org/10.64898/2026.04.21.720027; this version posted April 24, 2026. The copyright holder for this preprint (which was not certified by peer review) is the author/funder, who has granted bioRxiv a license to display the preprint in perpetuity. It is made available under a CC-BY-NC-ND 4.0 International license.

Endometrial PDO drug screening assay

PDOs were dissociated and singularized using TrpLE Express Enzyme as previously described, centrifuged at 300 g for 5 minutes at 4 °C, and resuspended in culture medium for cell counting. Cells were embedded in a 70:30 mixture of Matrigel:PDO culture medium at a density of 200 cells per µL. Ten microliter Matrigel domes were plated in 48-well or 384-well plates and allowed to polymerize for at least 5 minutes at 37 °C prior to addition of pre-warmed culture medium per well. PDOs were cultured until day 10 prior to drug exposure.

Drug-containing media or vehicle controls were added, and treatments were refreshed on day 13. PDO viability was quantified using the CellTiter-Glo® 3D Luminescent Cell Viability Assay (Promega, #G9682) according to the manufacturer's instructions on day 16. Briefly, culture media were aspirated and Matrigel domes were incubated with 100 µL CellTiter-Glo® 3D reagent for 30 minutes at 37°C in the dark. Lysates were transferred to opaque 96-well plates, and luminescence was measured using a SpectraMax plate reader. Luminescence values were normalized to vehicle-treated controls to determine relative viability. Per donor at least technical triplicates were used.

The following compounds were used: Carboplatin (10 nM-10 µM, Sigma Aldrich, #C2538), Paclitaxel (10 nM-10 µM, Thermo Fisher Scientific, #P3456), Carboplatin + Paclitaxel (31.25 nM-4 µM +312.5 nM-40 µM) A-485 (1 nM-10 µM , MedChemExpress, #HY-107455), 666-15 (1 nM-10 µM), MedChemExpress, #HY-101120), Verteporfin (6.25 nM-400 nM, Sigma Aldrich, #SML0534), Futibatinib (0.625 µM-50µM, MedChemExpress, #HY-100818R).

UCS PDOs bulk RNA-seq preparation and processing

PDOs were collected in Cell Recovery solution to dissolve Matrigel as previously described and afterwards lysed in 300 µl TRIzol (Zymo, #R2051). Then 300 µl 100 % ethanol (Fisher Scientific, #A4094) was added and the lysate transferred to a Zymo Spin Column and processed with the Direct-zol RNA protocol (Zymo, #R2051) according to manufacturer's instruction.

RNA depletion and library preparation was performed using NEBNext® Ultra II Directional RNA Library Prep Kit for Illumina® (Illumina, #E7765S/L) according to the manufacturer's protocol. Prepared library was analyzed using the Agilent Bioanalyzer 2100 using high sensitivity DNA chips (Agilent, #5067-4626). Sequencing was performed using NextSeq500.

Adapter sequences were removed from the FASTQ files using Cutadapt (v5.1). Obtained Cleaned and trimmed paired-end reads files were aligned and per-samples read counts were quantified

bioRxiv preprint doi: https://doi.org/10.64898/2026.04.21.720027; this version posted April 24, 2026. The copyright holder for this preprint (which was not certified by peer review) is the author/funder, who has granted bioRxiv a license to display the preprint in perpetuity. It is made available under a CC-BY-NC-ND 4.0 International license.

using STAR-2.5.1b with reference genome GRCh38. We used DESeq2 to perform differentially expression analysis between UCS PDOs and matched normals or biopsies. Significant DE genes were selected based on adjusted p-value (<0.05) and log-fold-change (±1.0) cutoffs. Obtained DE genes were subjected to functional enrichment analysis with human MSigDB hallmark gene sets (https://gsea-msigdb.org) and gene ontology (https://geneontology.org) using GeneSCF (v1.1-p3) tool[60]. The enriched gene sets are selected by p-value<0.05 cutoff.

Endometrial PDOs and tissue immunohistochemistry / Hematoxylin & eosin staining

Endometrial tissue specimens were fixed in 10 % formalin for 24-48 hours at room temperature. Following fixation, tissues were dehydrated through a graded ethanol series, cleared in xylene, and embedded in paraffin using standard histological procedures. Paraffin blocks were sectioned at 4 µm thickness using a microtome and mounted onto glass slides.

PDOs were collected in Cell Recovery Solution as previously described. The suspension was transferred into a tube pre-coated with 0.1 % BSA in PBS and incubated on ice for 10-15 min with gentle pipetting every 2-3 min until Matrigel was fully dissolved. Samples were centrifuged at 300 g for 5 min at 4 °C, and the supernatant was carefully removed. The PDO pellet was fixed in 4 % paraformaldehyde (PFA) for 30 minutes at room temperature. Following fixation, samples were centrifuged at 300 g for 5 min, washed twice with 1X PBS, and centrifuged again under the same conditions. After removal of PBS, PDOs were resuspended in 2 % low-melting-point agarose. The suspension was gently mixed and allowed to solidify at RT for 10 min. The solidified agarose block containing PDOs was transferred into a histology cassette, stored in 1X PBS, and embedded and sections as described above. Hematoxylin & eosin (H&E) stainings were performed according to standard protocols.

For immunohistochemistry (IHC) stainings, slides were stained in Discovery Ultra automatic IHC stainer (Roche) following standard protocols. Briefly, after deparaffinization and rehydration, slides were subjected to antigen retrieval (Benchmark Ultra CC1, Roche) at 96˚C for 64 minutes; primary Ab incubation was performed at 37 ˚C for 1h and Discovery multimer detection system (Discovery OmniMap HRP Roche) was used to detect and amplify immunosignals.

Primary antibodies used: E-cadherin (CST, #24E10), Ki67 (Spring Bioscience, #170822LVA), p53 (Thermo Fisher , #IHC-00010), EMA (Thermo Fisher, #Z2048MP).

bioRxiv preprint doi: https://doi.org/10.64898/2026.04.21.720027; this version posted April 24, 2026. The copyright holder for this preprint (which was not certified by peer review) is the author/funder, who has granted bioRxiv a license to display the preprint in perpetuity. It is made available under a CC-BY-NC-ND 4.0 International license.

TCGA UCS and P1000 UCS gene expression and copy number correlation

BIC-Seq2 (v0.2.6)[61] was run with default parameters to generate copy number log2 ratios., Additionally, tumor read depth was collected in 1KB bins and corrected for genomic GC content and mappability using fragCounter (https://github.com/mskilab/fragCounter). Corrected tumor coverage profiles, BAF, purity/ploidy estimates, and high confidence SVs were used as input to JaBbA (v1.1)[62] default parameters were used, with the exception of rescue.all set to false, maxna set to 0.8, slack of 1000 and ism set to true.

We compared *FGFR1* and *FGFR3* expression against log-transformed copy number values generated by JaBbA and BIC-Seq2. Gene expression (TPM) data were obtained from the P1000 endometrial (carcinosarcoma) and TCGA-UCS cohorts, with copy number estimates derived from both tools for each cohort. Expression-copy number associations were assessed by fitting linear models using lm() in R and R^2 values were reported separately per cohort. We obtained TCGA-UCS gene expression data from the published dataset available on CBioPortal[25,63]. Similarly copy number correlation with gene expression profiles of UCS PDOs from this study was done using afore mentioned method.

P1000 UCS tissue and PDOs whole genome sequencing

Library preparation

DNA was extracted from snap frozen patient tissue utilizing the Zymo Quick-DNA Miniprep kit (Zymo, #D3024) according to manufacturer's instruction. DNA quality and concentration were assessed using the Nanodrop ND-1000 Spectrophotometer. Whole genome sequencing (WGS) libraries were prepared using the Truseq DNA PCR-free Library Preparation Kit (Illumina) in accordance with the manufacturer's instructions. Briefly, 1 ug of DNA was sheared using a Covaris LE220 sonicator (adaptive focused acoustics). DNA fragments underwent bead-based size selection and were subsequently end-repaired, adenylated, and ligated to Illumina sequencing adapters. Final libraries were quantified using the Qubit Fluorometer (Life Technologies) or Spectromax M2 (Molecular Devices) and Fragment Analyzer (Advanced Analytical) or Agilent 2100 BioAnalyzer. Libraries were sequenced on an Illumina Novaseq6000 sequencer using 2x150bp cycles.

bioRxiv preprint doi: https://doi.org/10.64898/2026.04.21.720027; this version posted April 24, 2026. The copyright holder for this preprint (which was not certified by peer review) is the author/funder, who has granted bioRxiv a license to display the preprint in perpetuity. It is made available under a CC-BY-NC-ND 4.0 International license.

Processing and Analysis (Alignment, Variant calling, Filtering, Annotation)

Pre-processing

The New York Genome Center somatic pipeline (v6) was used to process and align the WGS data and call variants. Sequencing reads for the tumor and normal samples are aligned to the reference genome GRCh38 using BWA-MEM (v0.7.15) (arXiv:1303.3997v2 [q-bio.GN]). NYGC's ShortAlignmentMarking (v2.1) is used to mark short reads as unaligned. This tool is intended to remove spurious alignments resulting from contamination (e.g. saliva sample bacterial content) or from too aggressive alignments of short reads the size of BWA-MEM's 19bp minimum seed length. These spurious alignments result in pileups in certain locations of the genome and can lead to erroneous variant calling.

GATK (v4.1.0)[64] FixMateInformation is run to verify and fix mate-pair information, followed by Novosort (v1.03.01) markDuplicates to merge individual lane BAM files into a single BAM file per sample. Duplicates are then sorted and marked, and GATK's base quality score recalibration (BQSR) was performed. The result of the pre-processing pipeline is a coordinate sorted BAM file for each sample.

Quality control

Once preprocessing is complete, we compute several alignment quality metrics such as average coverage, %mapped reads and %duplicate reads using GATK (v4.1.0) and an autocorrelation metric (adapted for WGS from Zhang et al.[65]) to check for unevenness of coverage. We also run Conpair[66], a tool developed at NYGC to check the genetic concordance between the normal and the tumor sample and to estimate any inter-individual contamination in the samples.

Variant detection

The tumor and normal bam files are processed through NYGC's variant calling pipeline which consists of MuTect2 (GATK v4.0.5.1)[67], Strelka2 (v2.9.3)[68] and Lancet (v1.0.7)[69] for calling Single Nucleotide Variants (SNVs) and short Insertion-or-Deletion (Indels), SvABA (v0.2.1)[70] for calling Indels and Structural variants (SVs), Manta (v1.4.0)[71] and Lumpy (v0.2.13)[72] for calling SVs and BIC-Seq2 (v0.2.6)[61] for calling Copy-number variants (CNVs). Manta also outputs a candidate set of Indels which is provided as input to Strelka2 (following the developers recommendation, as it improves Strelka2's sensitivity for calling indels >20nt).

Variant merging

bioRxiv preprint doi: https://doi.org/10.64898/2026.04.21.720027; this version posted April 24, 2026. The copyright holder for this preprint (which was not certified by peer review) is the author/funder, who has granted bioRxiv a license to display the preprint in perpetuity. It is made available under a CC-BY-NC-ND 4.0 International license.

Next, the calls are merged by variant type (SNVs, Multi Nucleotide Variants (MNVs), Indels and SVs). MuTect2 and Lancet call MNVs, however Strelka2 does not, and it also does not provide any phasing information. So to merge such variants across callers, we first split the MNVs called by MuTect2 and Lancet to SNVs, and then merge the SNV callsets across the different callers. If the caller support for each SNV in a MNV is the same, we merge them back to MNVs. Otherwise those are represented as individual SNVs in the final callset. Lancet and MantaSV are the only tools that can call deletion-insertion (delins or COMPLEX) events. Other tools may represent the same event as separate yet adjacent indel and/or SNV variants. Such events are relatively less frequent, and difficult to merge. We therefore do not merge COMPLEX calls with SNVs and Indels calls from other callers. The SVs are converted to bedpe format, all SVs below 500bp are excluded and the rest are merged across callers using bedtools[73] pairtopair (slop of 300bp, same strand orientation, and 50% reciprocal overlap).

Somatic variant annotation (SNVs, Indels, CNVs, and SVs)

SNVs and Indels are annotated with Ensembl as well as databases such as COSMIC (v86)[74], 1000Genomes (Phase3)[75] , ClinVar (201706)[76], PolyPhen (v2.2.2)[77], SIFT (v5.2.2)[78], FATHMM (v2.1)[79], gnomAD (r2.0.1)[80] and dbSNP (v150)[81] using Variant Effect Predictor (v93.2)[82]. For CNVs, segments with log2 > 0.2 are categorized as amplifications, and segments with log2 < -0.235 are categorized as deletions (corresponding to a single copy change at 30% purity in a diploid genome, or a 15% Variant Allele Fraction). CNVs of size less than 20Mb are denoted as focal and the rest are considered large-scale.

We use bedtools[73] for annotating SVs and CNVs. All predicted CNVs are annotated with germline variants by overlapping with known variants in 1000 Genomes and Database of Genomic Variants (DGV) (22). Cancer-specific annotation includes overlap with genes from Ensembl[83] and Cancer Gene Census in COSMIC, and potential effect on gene structure (e.g. disruptive, intronic, intergenic). If a predicted SV disrupts two genes and strand orientations are compatible, the SV is annotated as a putative gene fusion candidate. Note that we do not check reading frame at this point. Further annotations include sequence features within breakpoint flanking regions, e.g. mappability, simple repeat content and segmental duplications.

Somatic Variant Filtering

Panel of normals (PON)

bioRxiv preprint doi: https://doi.org/10.64898/2026.04.21.720027; this version posted April 24, 2026. The copyright holder for this preprint (which was not certified by peer review) is the author/funder, who has granted bioRxiv a license to display the preprint in perpetuity. It is made available under a CC-BY-NC-ND 4.0 International license.

The Panel Of Normals (PON) filtering removes recurrent technical artifacts from the somatic variant callset[67].

PON generation

The Panel of Normals for SNVs, indels and SVs was created with whole-genome sequencing data from normal samples from 242 unrelated individuals. Of these, sequencing data for 148 individuals was obtained from the Illumina Polaris project which was sequenced on the HiSeqX2 platform with PCR-free sample preparation. The remaining samples were sequenced by the NYGC. Of these, 73 individuals were sequenced on HiSeqX, 11 on NovaSeq, and 10 were sequenced on both. We ran MuTect2 in artifact detection mode and Lumpy in single sample mode on these samples. For SNVs and indels, we created a PON list file with sites that were seen in two or more individuals.

For SVs, we used SURVIVOR (v1.0.3)[84] to merge Lumpy calls. Variants were merged if they were of the same type, had the same strand orientation, and were within 300bp of each other (maximum distance). We did not specify a minimum size. After merging SVs, we used these calls as a PON list.

PON filtering

For SNVs and Indels, we use the PON list to filter the somatic variants in the merged SNV and indel files. To filter our somatic SV callset, we merge our PON list with our callset using bedtools pairtopair (slop of 300bp, same strand orientation, and 50% reciprocal overlap), and filtered those SVs found in two or more individuals in our PON.

Common germline variants

In addition to the PON filtering, we remove SNVs and Indels that have minor allele frequency (MAF) of 1% or higher in either 1000Genomes (phase 3) or gnomAD (r2.0.1)[80], and SVs that overlap DGV and 1000Genomes (phase3). CNVs are annotated with DGV and 1000 Genomes but not filtered.

All somatic and high-confidence variants

Variants that pass all of the above-mentioned filters are included in our final somatic callset (hereby referred to as AllSomatic). For SNVs, indels and SVs, we also annotate a subset of the somatic callset as high confidence. For SNVs and indels, high confidence calls are defined as those that are either called by two or more variant callers or called by one caller and also seen in the Lancet validation calls or in the Manta SV calls.

bioRxiv preprint doi: https://doi.org/10.64898/2026.04.21.720027; this version posted April 24, 2026. The copyright holder for this preprint (which was not certified by peer review) is the author/funder, who has granted bioRxiv a license to display the preprint in perpetuity. It is made available under a CC-BY-NC-ND 4.0 International license.

For structural variants, high confidence calls are taken from the somatic callset if they meet the following criteria: called by 2 or more variant callers or called by Manta or Lumpy with either additional support from nearby CNV changepoint or split-read support from SplazerS[80], an independent tool used to calculate the number of split-reads supporting SV breakpoints. An SV is considered supported by SplazerS if it found at least 3 split-reads in the tumor only. Nearby CNV changepoints are determined by overlapping BIC-Seq2 calls with the SV callset using bedtools closest. An SV is supported by a CNV changepoint if the breakpoint of the CNV is within 1000bp of an SV breakpoint.

MSI detection

We run MANTIS (v1.0.4)[28] for Microsatellite Instability (MSI) detection in microsatellite loci (found using RepeatFinder, a tool included with MANTIS). A sample is considered to be 6 microsatellite unstable if it's Step-Wise Difference score reported by MANTIS is greater than 0.4 (or 0.62 in absence of a matched-normal). Otherwise, it is microsatellite stable3 (MSS).

Genetic ancestry estimation from whole genome

Ancestry proportion is determined by the software ADMIXTURE v1.3.0[26], which uses a maximum likelihood-based method to estimate the proportion of reference population ancestries in a sample. We genotyped the reference markers generated from 1,964 unrelated 1000 Genomes project samples directly on the samples using GATK pileup. Individuals from populations MXL (Mexican Ancestry from Los Angeles USA), ACB (African Caribbean in Barbados), and ASW (African Ancestry in Southwest US) were excluded from the reference due to being putatively admixed. The reference was further filtered by using only SNP markers with a minimum minor allele frequency (MAF) of 0.01 overall and 0.05 in at least one 1000 genomes superpopulation. Variants are additionally linkage disequilibrium (LD) pruned using PLINK v1.9 with a window size of 500kb, a step size of 250kb and r2 threshold of 0.2. The analysis results in a proportional breakdown of each sample into 5 continental populations (AFR, AMR, EAS, EUR, SAS) and 23 sub-populations.

bioRxiv preprint doi: https://doi.org/10.64898/2026.04.21.720027; this version posted April 24, 2026. The copyright holder for this preprint (which was not certified by peer review) is the author/funder, who has granted bioRxiv a license to display the preprint in perpetuity. It is made available under a CC-BY-NC-ND 4.0 International license.

UCS panel sequencing processing and variant calling

CSHL Next Generation Sequencing Core Facility performed capture based targeted gene panel sequencing (for a panel of potential cancer driver genes). Briefly, we initially used a panel of 143 cancer genes (based on the hg19 reference genome) with a total of ~4000 probes for capture. We later updated to a new panel of 163 genes (including all original genes) using ~7700 Twist probes based on the hg38 reference genome. The captured DNA was prepared into libraries using the Twist Library Preparation EF Kit 2.0 and Twist UDI TruSeq compatible adapters. Final captured libraries were sequenced on an Illumina NextSeq500 using paired-end 150bp reads to a coverage of ~100–300x.

UCS whole exome (WE) sequencing processing and variant calling

CSHL Next Generation Sequencing Core Facility prepared libraries with the KAPA HyperPlus Library Preparation kit. Briefly, gDNA was enzymatically fragmented in a thermal cycler for 30 minutes, followed by end repair and A-tailing. Illumina compatible dual indexes were ligated and libraries were amplified with 7 cycles of pcr enrichment, quantified by qubit and pooled equimolar. Following manufacturer protocol, libraries were hybridized to NimbleGen SeqCap EZ Library v3.0 probes[85] for 72 hours in a thermal cycler. Post hybridization, capture reactions were recovered and washed, followed by 12 cycles of post capture pcr enrichment. These post capture libraries were purified, and quantified with qubit and qpcr. Agilent tapestation was to determine insert fragment length. Post capture libraries were pooled and sequenced on an Illumina NextSeq500 PE150 high output run to ~75-100X coverage.

Whole exome sequences were aligned with Burrows-Wheeler Aligner (BWA) v0.7.17[86] (RRID:SCR_010910) to the human genome (GRCh38.p13 assembly). Picard v2.21.8 (http://broadinstitute.github.io/picard/) was used to removed duplicated sequences. A recalibration step was done with GATK v4.1.2.0[64].

Copy number variants (CNV) were identified with CNVkit v0.9.6[87]. The results were post-processed with CNprep[88] package v2.1.1 to calculate the copy number values relative to their central values for each segment (median deviation in log2ratio). Thresholds to assign a significant alteration were set to p-value < 0.001 for deletions and p-value > 0.999 for amplifications. The chromosomes Y and M have been removed from the analyses.

bioRxiv preprint doi: https://doi.org/10.64898/2026.04.21.720027; this version posted April 24, 2026. The copyright holder for this preprint (which was not certified by peer review) is the author/funder, who has granted bioRxiv a license to display the preprint in perpetuity. It is made available under a CC-BY-NC-ND 4.0 International license.

686 **Mutational analysis**

687 The sequencing reads were aligned to the hg19 or hg38 reference genome (depending upon capture
688 probes used) using BWA[89], followed by BAM formatting and sorting with Samtools[90]. PCR
689 duplicates were removed with Picard (https://broadinstitute.github.io/picard/), and Bamtools[91] was
690 used to select a minimum mapping quality of 20 and proper read pairing. Coverage of the target
691 regions was assessed using Picard HSmetrics to ensure adequate coverage for confident variant
692 detection. Variants were called using VarScan2[92] in somatic mode to stratify germline versus
693 somatic variants. Resulting variants were annotated with Annovar[93] to cover a broad range of
694 prediction tools. We selected rare loss of function variants (nonsense, frameshift, splice site) with
695 frequency less than 1% in the Gnomad, ExAC, EVS and 1000 Genomes databases. Missense and
696 in-frame indel variants were selected if they were noted as pathogenic by ClinVar[94], or if they were
697 both rare and present in COSMIC[74], or if they are both rare and found to be present in the TCGA
698 cohorts.
699 In order to harmonize variants between captures, we used the liftOver tool from the UCSC Genome
700 Browser to convert coordinates form hg19 to hg38.
701 Oncoplots are generated from these candidate variants using Maftools[95].
702

703 **UCS whole genome (SMASH) sequencing processing**

704 SMASH sequencing data were processed using a custom SMASH Analytics pipeline developed
705 in-house, as previously described[96], with implementation available at
706 https://github.com/docpaa/smash-paper. Sequencing reads were aligned to the human reference
707 genome (hg19 assembly).
708 Copy number variants (CNV) were detected using CNprep[88] package v2.1.1 to obtain the median
709 deviation in log2ratio. Thresholds to assign a significant alteration were set to p-value < 0.001 for
710 deletions and p-value > 0.999 for amplifications. The chromosomes Y and M have been removed
711 from the analyses. The graphical representation of the amplification and deletion events through
712 the genome has been generated with the Bioconductor gtrellis[97] package v1.28.0.
713

714 **UCS PDOs-tumor CNV comparison in whole exome and SMASH**

715 Similarity between copy number profiles has been calculated with Bioconductor CNVMetrics[98,99]
716 package v1.6.0. The copy number profiles, deletion and amplification separated in different sets,

bioRxiv preprint doi: https://doi.org/10.64898/2026.04.21.720027; this version posted April 24, 2026. The copyright holder for this preprint (which was not certified by peer review) is the author/funder, who has granted bioRxiv a license to display the preprint in perpetuity. It is made available under a CC-BY-NC-ND 4.0 International license.

were used as input. For each pair of profiles, the Sørensen coefficient is used as the similarity measure. The Sørensen coefficient is obtained by dividing twice the size of the intersection of the amplified/deleted regions by the sum of the size of the amplified/deleted regions for the two profiles. For each pair of profiles, 500 synthetic profiles were generated for one profile of the pair (when a metric could not be successfully calculated with a synthetic profile, the synthetic profile was discarded). The p-value was obtained by calculating the ratio of synthetic profiles with equal or higher coefficient that the one obtained with the real pair of profiles (one observation is always added to the calculation).

The similarity heatmaps were generated with Bioconductor ComplexHeatmap[97] package v2.12.0 using the Euclidean distance and the complete method for clustering.

Analyzing somatic variants and ancestry using scRNA-seq from UCS PDOs

First, FASTQ files were extracted from scRNA-seq alignment done on cellranger from 10X Chromium using GRCh38 2016 release 84 reference and converted BAM files to FASTQ with the help of 10X bamtofastq software version 1.4.1 (https://support.10xgenomics.com/docs/bamtofastq). The FASTQ files were used as input to generate new alignments on 10X Chromium GRCh38 2020A reference with 10X Chromium cellranger software version 7.0.0[100]. Those alignments are used for further processing. Variant calling was done following the GATK RNA-seq Best Practices[64] except for the duplicate removal step which was skipped. The first steps of the pipeline were run with GATK software version 4.2.5.0, and the final output was the recalibrated BAM files. At last, Picard software version 2.26.11 (https://broadinstitute.github.io/picard/) was used to resort the BAM files according to GENCODE version 39 genome order[101]. Somatic variants were extracted for each cell with both SCExecute software version 1.3.2[102] and snp-pileup tool from FACETS software version 0.6.1 (Shen et al 2016). The list of somatic variants used as input was specific to each PDO samples as obtained for the variant calling done on the exome sequencing.

Genetic ancestry on scRNA-seq was done with RAIDS software v0.99.15 following the pipeline presented in Belleau et al. 2023[103] with the inference step changed from principal-component analysis to admixture analysis with ADMIXTURE software version 1.3.0[26]. The list of variants used as input was obtained with snp-pileup tool from FACETS software version 0.6.1[104] run on the recalibrated BAM files directly.

bioRxiv preprint doi: https://doi.org/10.64898/2026.04.21.720027; this version posted April 24, 2026. The copyright holder for this preprint (which was not certified by peer review) is the author/funder, who has granted bioRxiv a license to display the preprint in perpetuity. It is made available under a CC-BY-NC-ND 4.0 International license.

UCS single cell profiling by Chromium 10X sequencing and analysis

For cell isolation from endometrial tissue, samples were processed as described above for endometrial tissue processing and PDOs generation. Following termination of trypsin digestion and centrifugation, cell pellets were resuspended in 3 mL of fresh ADMEM/F12 and filtered through a 40 µm cell strainer (Corning, #431750). Dead cells were subsequently removed using the Dead Cell Removal Kit (Miltenyi Biotec, #130-090-101) according to the manufacturer's instructions using a MACS separation system. Final cell suspensions exhibited 80-90% viability with yields of at least1.5 million cells.

PDO lines maintained for at least two passages after thawing or initial establishment were harvested for single-cell preparation. Matrigel was dissolved by incubating PDOs in Cell Recovery Solution for 1 h at 4 °C. PDOs were washed and enzymatically dissociated using TrypLE Express for 10-45 min, with gentle mechanical trituration by pipetting every 5 min to promote generation of single cells. Digestion was monitored by brightfield microscopy and quenched by dilution with serum-free culture medium once an adequate fraction of single cells was observed. Cell suspensions were filtered through a 40 µm strainer, pelleted, and resuspended in ADMEM/F12. Dead cells were removed using the Dead Cell Removal Kit according to the manufacturer's instructions. Final preparations typically yielded in over 1.5 million cells with 80-90% viability.

Samples are processed for sequencing with Chromium Next GEM Chip G (10x Genomics). GEM generation and barcoding, reverse transcription, cDNA generation and library construction using 3′ Gene Expression Library Construction using the Chromium Single Cell 30 Library (v3 chemistry) following the manufacturer's protocol. Dual-indexed, single-cell libraries were pooled and sequenced in paired-end reads on Novaseq (Illumina).

Single-cell analysis

Raw reads from FASTQ files are aligned to reference genome GRCh38 and quantified for GRCh38.84 gene annotation using CellRanger (v.6.0.0) (https://10xgenomics.com). First, the CellRanger *mkfastq* command with the CellRanger sample sheet was used to demultiplex the base call files for each flow cell into FASTQ files. Second, the CellRanger *count* command was called to generate single cell feature counts for each library by specifying the library name in the argument. The filtered feature barcode matrix was used for further data analysis.

bioRxiv preprint doi: https://doi.org/10.64898/2026.04.21.720027; this version posted April 24, 2026. The copyright holder for this preprint (which was not certified by peer review) is the author/funder, who has granted bioRxiv a license to display the preprint in perpetuity. It is made available under a CC-BY-NC-ND 4.0 International license.

Quality check and clustering

The downstream analysis using feature barcode matrix was performed using Seurat (v.3.0.0) package. Individual patients with their feature barcode matrix libraries were converted into Seurat object using *Read10X* and *CreateSeuratObject*. For each individual patients we removed cells with high mitochondrial content (>20%) and cells with less than 200 genes. These cut-offs are based on QC inspection and previous single cell studies on endometrium[10536,95]. Subsequently, the gene in remaining 97,622 cells were log normalized, variable genes detected, scaled and the principal components computed. The top principal components were identified and used for the UMAP and TSNE dimensionality reduction. Normal endometrium singe cell data from Wang et al.[105], was filtered using the cutoffs mentioned in the publication and the clustering is performed like CS patients.

Heterogeneity and assignment of cell types

Initial clustering was performed, and CS patients showed highly heterogenous profiles. Individual clusters are assigned to a patient based on proportion of cells from the patient contributing to the cluster. Hence on the gene markers are predicted per cluster in individual CS patient by *FindAllMarkers* function from Seurat. This method of assigning gene markers and cell types preserved both molecular and cellular-level heterogeneity in CS patients. Similar approach was used in prediction of gene markers and cell type assignment for normal endometrium singe cell data from Wang et al. Scoring of cells for different functional modules are done using *AddModuleScore_UCell* function from UCell R package.

UCS single cell differential expression analysis

Differential expression (DE) analysis between normal endometrium and CS predicted cancer cells were performed by implementing Libra using *run_de* function (https://github.com/neurorestore/Libra)[106]. We used single cell appropriate statistical method Wilcoxon Rank-Sum test to find differentially expressed genes. Similarly, DE analysis was performed between CS primary and metastatic stages, between normal endometrium immune profile and CS tumor infiltrating immune profile. Significant DE genes were selected based on adjusted p-value (<0.05) and log-fold-change (±1.0) cutoffs. Obtained DE genes were subjected to functional enrichment analysis with human MSigDB hallmark gene sets (https://gsea-

bioRxiv preprint doi: https://doi.org/10.64898/2026.04.21.720027; this version posted April 24, 2026. The copyright holder for this preprint (which was not certified by peer review) is the author/funder, who has granted bioRxiv a license to display the preprint in perpetuity. It is made available under a CC-BY-NC-ND 4.0 International license.

msigdb.org) and gene ontology (https://geneontology.org) using GeneSCF (v1.1-p3) tool[60]. The enriched gene sets are selected by p-value<0.05 cutoff.

UCS promoter sequence based motif enrichment analysis

Using custom scripts we extracted nucleotide sequences (FASTA) from the promoters (± 250 bp from TSS) of list of significantly differentially expressed genes between CS predicted cancer cells and normal endometrium (https://github.com/decodebiology/extract_promoter_sequence) with GRCh38.84 gene and genome annotation. Obtained FASTA sequences were used to find enriched transcription factor motifs using SEA (v5.5.5) from MEME tool. Motif database HOCOMOCO (v11) full human was used, and the shuffled primary sequences preserving 3-mer frequencies are considered as control sequences. Also, 10% of the input sequences were randomly assigned to the hold-out set to improve p-value accuracy. The motifs are selected based on enrichment E-value of 10 or smaller. Motifs analysis was performed independently on both up and downregulated genes.

Data and Code Availability

All sample data has been deposited to GEO and dbGAP and can be accessed upon request.

Acknowledgements

We thank the members of the Beyaz lab for critical discussions. We thank Northwell Health Biospecimen Repository and the Gynecologic Oncology staff for assistance in recruitment of patients from diverse demographics and acquisition of specimens for this study. We thank Cold Spring Harbor Laboratory Cancer Center Shared Resources (Flow Cytometry, Microscopy, Sequencing, Organoid and Histology Core Facilities) supported in part by the National Cancer Institute Cancer Center Support Grant (5P30CA045508). This work was financially supported by grants to S.B. from the National Cancer Institute (R37CA292807), Oliver S. and Jennie R. Donaldson Charitable Trust, the Mark Foundation for Cancer Research (20-028-EDV), the Cold Spring Harbor Laboratory and Northwell Health Affiliation, New York Genome Center Polyethnic-1000 Initiative. This work was performed with assistance from the US National Institutes of Health Grant S10OD028632-01. The results shown here are in part based upon data generated by the TCGA Research Network: https://www.cancer.gov/tcga. P.B. is supported by the National Cancer Institute's Informatics Technology for Cancer Research (ITCR) program Grant U01CA289357. The sample processing, computations, and depositions of the datasets from this

bioRxiv preprint doi: https://doi.org/10.64898/2026.04.21.720027; this version posted April 24, 2026. The copyright holder for this preprint (which was not certified by peer review) is the author/funder, who has granted bioRxiv a license to display the preprint in perpetuity. It is made available under a CC-BY-NC-ND 4.0 International license.

840 study and TCGA was performed on High Performance Computing (HPC) resources Elzar and
841 Agastya provided by Cold Spring Harbor Laboratory and Indian Institute of Technology Jammu
842 respectively.

bioRxiv preprint doi: https://doi.org/10.64898/2026.04.21.720027; this version posted April 24, 2026. The copyright holder for this preprint (which was not certified by peer review) is the author/funder, who has granted bioRxiv a license to display the preprint in perpetuity. It is made available under a CC-BY-NC-ND 4.0 International license.

References

1. Bogani, G. *et al.* Endometrial carcinosarcoma. *Int. J. Gynecol. Cancer* **33**, 147–174 (2023).
2. Maiorano, M. F., Cormio, G., Maiorano, B. A. & Loizzi, V. Uterine Carcinosarcoma (UCS): A Literature Review and Survival Analysis from a Retrospective Cohort Study. *Cancers* **16**, 3905 (2024).
3. Gopinatha Pillai, M. S. *et al.* Uterine carcinosarcoma: Unraveling the role of epithelial-to-mesenchymal transition in progression and therapeutic potential. *FASEB J.* **38**, e70132 (2024).
4. Beliaeva, A. & Bakhidze, E. Diagnosis and treatment of uterine carcinosarcoma. *J. Clin. Oncol.* **38**, e18111–e18111 (2020).
5. Tung, H.-J. *et al.* Management and Prognosis of Patients with Recurrent or Persistent/Progressive Uterine Carcinosarcoma. *Curr. Oncol.* **29**, 7607–7623 (2022).
6. Powell, M. A. *et al.* Randomized Phase III Trial of Paclitaxel and Carboplatin Versus Paclitaxel and Ifosfamide in Patients With Carcinosarcoma of the Uterus or Ovary: An NRG Oncology Trial. *J. Clin. Oncol.* **40**, 968–977 (2022).
7. Mahdi, H. *et al.* Evolving treatment paradigms in metastatic or recurrent low-grade endometrial cancer: When is hormonal-based therapy the preferred option? *Int. J. Gynecol. Cancer Off. J. Int. Gynecol. Cancer Soc.* **33**, 1675–1681 (2023).
8. Pham, E. N. B. *et al.* Quality of life and survival in patients with uterine carcinosarcoma: A tertiary center observational study. *Gynecol. Oncol. Rep.* **57**, 101679 (2025).
9. Pham, E. N. B. *et al.* Molecular diversity in uterine carcinosarcoma: Beyond TP53. *Gynecol. Oncol.* **198**, 75–83 (2025).
10. Gotoh, O. *et al.* Clinically relevant molecular subtypes and genomic alteration-independent differentiation in gynecologic carcinosarcoma. *Nat. Commun.* **10**, 4965 (2019).

bioRxiv preprint doi: https://doi.org/10.64898/2026.04.21.720027; this version posted April 24, 2026. The copyright holder for this preprint (which was not certified by peer review) is the author/funder, who has granted bioRxiv a license to display the preprint in perpetuity. It is made available under a CC-BY-NC-ND 4.0 International license.

11. Kandoth, C. *et al.* Integrated genomic characterization of endometrial carcinoma. *Nature* **497**, 67–73 (2013).

12. Lee, M.-K. *et al.* Cumulative abdominal obesity exposure and progressive risk of endometrial cancer in young women: a nationwide cohort study. *Int. J. Obes.* **49**, 2094–2101 (2025).

13. Liao, C.-I. *et al.* Increasing incidence of uterine carcinosarcoma: A United States Cancer Statistics study. *Gynecol. Oncol. Rep.* **40**, 100936 (2022).

14. Abel, M. K. *et al.* Racial disparities in high-risk uterine cancer histologic subtypes: A United States Cancer Statistics study. *Gynecol. Oncol.* **161**, 470–476 (2021).

15. Ben-David, U. *et al.* Genetic and transcriptional evolution alters cancer cell line drug response. *Nature* **560**, 325–330 (2018).

16. Collins, A. *et al.* Patient-derived explants, xenografts and organoids: 3-dimensional patient-relevant pre-clinical models in endometrial cancer. *Gynecol. Oncol.* **156**, 251–259 (2020).

17. Maenhoudt, N., De Moor, A. & Vankelecom, H. Modeling Endometrium Biology and Disease. *J. Pers. Med.* **12**, (2022).

18. Xue, Y. *et al.* Preclinical research models for endometrial cancer: development and selection of animal models. *Front. Oncol.* **15**, 1512616 (2025).

19. Clevers, H. Modeling Development and Disease with Organoids. *Cell* **165**, 1586–1597 (2016).

20. Maru, Y. *et al.* Establishment and characterization of multiple patient-derived organoids from a case of advanced endometrial cancer. *Hum. Cell* **37**, 840–853 (2024).

bioRxiv preprint doi: https://doi.org/10.64898/2026.04.21.720027; this version posted April 24, 2026. The copyright holder for this preprint (which was not certified by peer review) is the author/funder, who has granted bioRxiv a license to display the preprint in perpetuity. It is made available under a CC-BY-NC-ND 4.0 International license.

888 21. Dahl, M. J. *et al.* Gemcitabine combination therapies induce apoptosis in uterine
889 carcinosarcoma patient-derived organoids. *Front. Oncol.* **14**, 1368592 (2024).
890 22. Moufarrij, S. *et al.* TROP2 as a novel target in uterine carcinosarcoma organoid models.
891 *Gynecol. Oncol.* **190**, S204 (2024).
892 23. Park, A. B. *et al.* Racial disparities in survival among women with endometrial cancer in
893 an equal access system. *Gynecol. Oncol.* **163**, 125–129 (2021).
894 24. Long, B., Liu, F. W. & Bristow, R. E. Disparities in uterine cancer epidemiology,
895 treatment, and survival among African Americans in the United States. *Gynecol. Oncol.* **130**,
896 652–659 (2013).
897 25. Cherniack, A. D. *et al.* Integrated Molecular Characterization of Uterine Carcinosarcoma.
898 *Cancer Cell* **31**, 411–423 (2017).
899 26. Alexander, D. H., Novembre, J. & Lange, K. Fast model-based estimation of ancestry in
900 unrelated individuals. *Genome Res.* **19**, 1655–1664 (2009).
901 27. Maiorano, M. F. P., Cormio, G., Maiorano, B. A. & Loizzi, V. Uterine Carcinosarcoma
902 (UCS): A Literature Review and Survival Analysis from a Retrospective Cohort Study.
903 *Cancers* **16**, (2024).
904 28. Kautto, E. A. *et al.* Performance evaluation for rapid detection of pan-cancer
905 microsatellite instability with MANTIS. *Oncotarget* **8**, 7452–7463 (2017).
906 29. Katcher, A. *et al.* Establishing patient-derived organoids from human endometrial cancer
907 and normal endometrium. *Front. Endocrinol.* **14**, 1059228 (2023).
908 30. Barbi, M. *et al.* Generation and Maintenance of Patient-Derived Endometrial Cancer
909 Organoids. *Bio-Protoc.* **14**, e5093 (2024).

bioRxiv preprint doi: https://doi.org/10.64898/2026.04.21.720027; this version posted April 24, 2026. The copyright holder for this preprint (which was not certified by peer review) is the author/funder, who has granted bioRxiv a license to display the preprint in perpetuity. It is made available under a CC-BY-NC-ND 4.0 International license.

910 31. Boretto, M. *et al.* Patient-derived organoids from endometrial disease capture clinical
911 heterogeneity and are amenable to drug screening. *Nat. Cell Biol.* **21**, 1041–1051 (2019).
912 32. Ornitz, D. M. & Itoh, N. The Fibroblast Growth Factor signaling pathway. *Wiley*
913 *Interdiscip. Rev. Dev. Biol.* **4**, 215–266 (2015).
914 33. ElHarouni, D., Al-Jazrawe, M., Choi, S., Dede, M., Hinoue, T., Misek, S. A., Noh, H.,
915 Zanella, L., Tseng, Y.-Y., Francies, H. E., Plenker, D., Kyi, C. W., Perez-Mayoral, J., Stine,
916 M. J., Tonsing-Carter, E., Agarwal, R., Zenklusen, J. C., Clinton, J. M., Shelton, J. M., Chu,
917 T. R., Hooper, W. F., Loinaz, X., Keskula, P., Lee, J. A., Kuhlers, P. C., Tercan, B., Boj, S. F.,
918 Vasciaveo, A., Tomassoni, L., Crawford, J. M., Walsh, S., Sinai, C., Bhatia, S., Sridevi, P.,
919 Patel, H., Cerone, M. A., The HCMI Network, Ellrott, K., Kuo, C. J., Elemento, O., Beyaz, S.,
920 Corbo, V., Spector, D. L., Beroukhim, R., Ferguson, M. L., Cherniack, A. D., Laird, P. W.,
921 Robine, N., McPherson, A., Hoadley, K. A., Garnett, M. J., Tuveson, D. A., Califano, A.,
922 Spellman, P. T., Ligon, K. L., Gerhard, D. S., Staudt, L. M., Boehm, J. S. A compendium of
923 next-generation patient-derived models for diverse cancers.
924 34. Murali, R. *et al.* High-grade Endometrial Carcinomas: Morphologic and
925 Immunohistochemical Features, Diagnostic Challenges and Recommendations. *Int. J.*
926 *Gynecol. Pathol. Off. J. Int. Soc. Gynecol. Pathol.* **38 Suppl 1**, S40–S63 (2019).
927 35. Zhao, S. *et al.* Mutational landscape of uterine and ovarian carcinosarcomas implicates
928 histone genes in epithelial-mesenchymal transition. *Proc. Natl. Acad. Sci. U. S. A.* **113**,
929 12238–12243 (2016).
930 36. Zakrzewski, P. K. Canonical TGFβ Signaling and Its Contribution to Endometrial Cancer
931 Development and Progression-Underestimated Target of Anticancer Strategies. *J. Clin. Med.*
932 **10**, (2021).

bioRxiv preprint doi: https://doi.org/10.64898/2026.04.21.720027; this version posted April 24, 2026. The copyright holder for this preprint (which was not certified by peer review) is the author/funder, who has granted bioRxiv a license to display the preprint in perpetuity. It is made available under a CC-BY-NC-ND 4.0 International license.

933 37. Alexander, D. H., Novembre, J. & Lange, K. Fast model-based estimation of ancestry in
934 unrelated individuals. *Genome Res.* **19**, 1655–1664 (2009).
935 38. Chan John K. *et al.* Weekly vs. Every-3-Week Paclitaxel and Carboplatin for Ovarian
936 Cancer. *N. Engl. J. Med.* **374**, 738–748.
937 39. Miller, D. S. *et al.* Carboplatin and Paclitaxel for Advanced Endometrial Cancer: Final
938 Overall Survival and Adverse Event Analysis of a Phase III Trial (NRG
939 Oncology/GOG0209). *J. Clin. Oncol. Off. J. Am. Soc. Clin. Oncol.* **38**, 3841–3850 (2020).
940 40. Lee, M. X. & Tan, D. S. Weekly versus 3-weekly paclitaxel in combination with
941 carboplatin in advanced ovarian cancer: which is the optimal adjuvant chemotherapy
942 regimen? *J. Gynecol. Oncol.* **29**, e96 (2018).
943 41. Quintanal-Villalonga, Á. *et al.* Lineage plasticity in cancer: a shared pathway of
944 therapeutic resistance. *Nat. Rev. Clin. Oncol.* **17**, 360–371 (2020).
945 42. Pastushenko, I. & Blanpain, C. EMT Transition States during Tumor Progression and
946 Metastasis. *Trends Cell Biol.* **29**, 212–226 (2019).
947 43. Khanbabaei, H. *et al.* Non-coding RNAs and epithelial mesenchymal transition in cancer:
948 molecular mechanisms and clinical implications. *J. Exp. Clin. Cancer Res. CR* **41**, 278 (2022).
949 44. Han, P. & Chang, C.-P. Long non-coding RNA and chromatin remodeling. *RNA Biol.* **12**,
950 1094–1098 (2015).
951 45. Mitra, R. *et al.* Decoding critical long non-coding RNA in ovarian cancer epithelial-to-
952 mesenchymal transition. *Nat. Commun.* **8**, 1604 (2017).
953 46. Mehra, S., Singh, S. & Nagathihalli, N. Emerging Role of CREB in Epithelial to
954 Mesenchymal Plasticity of Pancreatic Cancer. *Front. Oncol.* **12**, 925687 (2022).

bioRxiv preprint doi: https://doi.org/10.64898/2026.04.21.720027; this version posted April 24, 2026. The copyright holder for this preprint (which was not certified by peer review) is the author/funder, who has granted bioRxiv a license to display the preprint in perpetuity. It is made available under a CC-BY-NC-ND 4.0 International license.

955 47. Yin, Y. *et al.* The CRTC-CREB axis functions as a transcriptional sensor to protect
956 against proteotoxic stress in Drosophila. *Cell Death Dis.* **13**, 688 (2022).
957 48. Hong, J. *et al.* cAMP response element–binding protein: A credible cancer drug target. *J.*
958 *Pharmacol. Exp. Ther.* **392**, (2025).
959 49. Wang, J. *et al.* CREB up-regulates long non-coding RNA, HULC expression through
960 interaction with microRNA-372 in liver cancer. *Nucleic Acids Res.* **38**, 5366–5383 (2010).
961 50. Jiang, L.-Y. *et al.* CREB-induced LINC00473 promotes chemoresistance to TMZ in
962 glioblastoma by regulating O6-methylguanine-DNA-methyltransferase expression via CEBPα
963 binding. *Neuropharmacology* **243**, 109790 (2024).
964 51. Ilyas, S. I. *et al.* A Hippo and Fibroblast Growth Factor Receptor Autocrine Pathway in
965 Cholangiocarcinoma. *J. Biol. Chem.* **291**, 8031–8047 (2016).
966 52. Turner, N. *et al.* FGFR1 amplification drives endocrine therapy resistance and is a
967 therapeutic target in breast cancer. *Cancer Res.* **70**, 2085–2094 (2010).
968 53. Dieci, M. V., Arnedos, M., Andre, F. & Soria, J. C. Fibroblast growth factor receptor
969 inhibitors as a cancer treatment: from a biologic rationale to medical perspectives. *Cancer*
970 *Discov.* **3**, 264–279 (2013).
971 54. Sawayama, S. *et al.* Efficacy of pazopanib in FGFR1-amplified uterine carcinosarcoma:
972 A case report. *Gynecol. Oncol. Rep.* **41**, 100993 (2022).
973 55. Sengal, A. T. *et al.* Endometrial cancer PDX-derived organoids (PDXOs) and PDXs with
974 FGFR2c isoform expression are sensitive to FGFR inhibition. *Npj Precis. Oncol.* **7**, 127
975 (2023).

bioRxiv preprint doi: https://doi.org/10.64898/2026.04.21.720027; this version posted April 24, 2026. The copyright holder for this preprint (which was not certified by peer review) is the author/funder, who has granted bioRxiv a license to display the preprint in perpetuity. It is made available under a CC-BY-NC-ND 4.0 International license.

976 56. Grant, G. & Ferrer, C. M. The role of the immune tumor microenvironment in shaping
977 metastatic dissemination, dormancy, and outgrowth. *Trends Cell Biol.*
978 https://doi.org/10.1016/j.tcb.2025.05.006 doi:10.1016/j.tcb.2025.05.006.
979 57. Anderson, N. M. & Simon, M. C. The tumor microenvironment. *Curr. Biol. CB* **30**,
980 R921–R925 (2020).
981 58. Raghavan, S. *et al.* Microenvironment drives cell state, plasticity, and drug response in
982 pancreatic cancer. *Cell* **184**, 6119-6137.e26 (2021).
983 59. Chung, C. *et al.* Ancestrally Diverse Autologous Patient-Derived Organoid–Immune Cell
984 Coculture Platform for Addressing Immunotherapeutic Outcome Disparities in High-Grade
985 Endometrial Cancer. *Cancer Res. Commun.* **6**, 657–671 (2026).
986 60. Subhash, S. & Kanduri, C. GeneSCF: a real-time based functional enrichment tool with
987 support for multiple organisms. *BMC Bioinformatics* **17**, 365 (2016).
988 61. Xi, R., Lee, S., Xia, Y., Kim, T.-M. & Park, P. J. Copy number analysis of whole-
989 genome data using BIC-seq2 and its application to detection of cancer susceptibility variants.
990 *Nucleic Acids Res.* **44**, 6274–6286 (2016).
991 62. Hadi, K. *et al.* Distinct Classes of Complex Structural Variation Uncovered across
992 Thousands of Cancer Genome Graphs. *Cell* **183**, 197-210.e32 (2020).
993 63. Cerami, E. *et al.* The cBio cancer genomics portal: an open platform for exploring
994 multidimensional cancer genomics data. *Cancer Discov.* **2**, 401–404 (2012).
995 64. McKenna, A. *et al.* The Genome Analysis Toolkit: a MapReduce framework for
996 analyzing next-generation DNA sequencing data. *Genome Res.* **20**, 1297–1303 (2010).
997 65. Zhang, L. & Zhang, L. Use of autocorrelation scanning in DNA copy number analysis.
998 *Bioinforma. Oxf. Engl.* **29**, 2678–2682 (2013).

bioRxiv preprint doi: https://doi.org/10.64898/2026.04.21.720027; this version posted April 24, 2026. The copyright holder for this preprint (which was not certified by peer review) is the author/funder, who has granted bioRxiv a license to display the preprint in perpetuity. It is made available under a CC-BY-NC-ND 4.0 International license.

66. Bergmann, E. A., Chen, B.-J., Arora, K., Vacic, V. & Zody, M. C. Conpair: concordance and contamination estimator for matched tumor-normal pairs. *Bioinforma. Oxf. Engl.* **32**, 3196–3198 (2016).

67. Cibulskis, K. *et al.* Sensitive detection of somatic point mutations in impure and heterogeneous cancer samples. *Nat. Biotechnol.* **31**, 213–219 (2013).

68. Kim, S. *et al.* Strelka2: fast and accurate calling of germline and somatic variants. *Nat. Methods* **15**, 591–594 (2018).

69. Narzisi, G. *et al.* Genome-wide somatic variant calling using localized colored de Bruijn graphs. *Commun. Biol.* **1**, 20 (2018).

70. Wala, J. A. *et al.* SvABA: genome-wide detection of structural variants and indels by local assembly. *Genome Res.* **28**, 581–591 (2018).

71. Chen, X. *et al.* Manta: rapid detection of structural variants and indels for germline and cancer sequencing applications. *Bioinforma. Oxf. Engl.* **32**, 1220–1222 (2016).

72. Layer, R. M., Chiang, C., Quinlan, A. R. & Hall, I. M. LUMPY: a probabilistic framework for structural variant discovery. *Genome Biol.* **15**, R84 (2014).

73. Quinlan, A. R. & Hall, I. M. BEDTools: a flexible suite of utilities for comparing genomic features. *Bioinforma. Oxf. Engl.* **26**, 841–842 (2010).

74. Tate, J. G. *et al.* COSMIC: the Catalogue Of Somatic Mutations In Cancer. *Nucleic Acids Res.* **47**, D941–D947 (2019).

75. Auton, A. *et al.* A global reference for human genetic variation. *Nature* **526**, 68–74 (2015).

76. Landrum, M. J. *et al.* ClinVar: public archive of relationships among sequence variation and human phenotype. *Nucleic Acids Res.* **42**, D980-985 (2014).

bioRxiv preprint doi: https://doi.org/10.64898/2026.04.21.720027; this version posted April 24, 2026. The copyright holder for this preprint (which was not certified by peer review) is the author/funder, who has granted bioRxiv a license to display the preprint in perpetuity. It is made available under a CC-BY-NC-ND 4.0 International license.

1022 77. Adzhubei, I., Jordan, D. M. & Sunyaev, S. R. Predicting functional effect of human
1023 missense mutations using PolyPhen-2. *Curr. Protoc. Hum. Genet.* **Chapter 7**, Unit7.20
1024 (2013).
1025 78. Vaser, R., Adusumalli, S., Leng, S. N., Sikic, M. & Ng, P. C. SIFT missense predictions
1026 for genomes. *Nat. Protoc.* **11**, 1–9 (2016).
1027 79. Shihab, H. A. *et al.* Ranking non-synonymous single nucleotide polymorphisms based on
1028 disease concepts. *Hum. Genomics* **8**, 11 (2014).
1029 80. Lek, M. *et al.* Analysis of protein-coding genetic variation in 60,706 humans. *Nature*
1030 **536**, 285–291 (2016).
1031 81. Sherry, S. T. *et al.* dbSNP: the NCBI database of genetic variation. *Nucleic Acids Res.* **29**,
1032 308–311 (2001).
1033 82. McLaren, W. *et al.* The Ensembl Variant Effect Predictor. *Genome Biol.* **17**, 122 (2016).
1034 83. Hubbard, T. *et al.* The Ensembl genome database project. *Nucleic Acids Res.* **30**, 38–41
1035 (2002).
1036 84. Jeffares, D. C. *et al.* Transient structural variations have strong effects on quantitative
1037 traits and reproductive isolation in fission yeast. *Nat. Commun.* **8**, 14061 (2017).
1038 85. Chen, R., Im, H. & Snyder, M. Whole-Exome Enrichment with the Roche NimbleGen
1039 SeqCap EZ Exome Library SR Platform. *Cold Spring Harb. Protoc.* **2015**, pdb.prot084855
1040 (2015).
1041 86. Li, H. & Durbin, R. Fast and accurate short read alignment with Burrows-Wheeler
1042 transform. *Bioinforma. Oxf. Engl.* **25**, 1754–1760 (2009).

bioRxiv preprint doi: https://doi.org/10.64898/2026.04.21.720027; this version posted April 24, 2026. The copyright holder for this preprint (which was not certified by peer review) is the author/funder, who has granted bioRxiv a license to display the preprint in perpetuity. It is made available under a CC-BY-NC-ND 4.0 International license.

1043 87. Talevich, E., Shain, A. H., Botton, T. & Bastian, B. C. CNVkit: Genome-Wide Copy
1044 Number Detection and Visualization from Targeted DNA Sequencing. *PLoS Comput. Biol.*
1045 **12**, e1004873 (2016).
1046 88. Belleau, P., Deschenes, A., Sun, G., Tuveson, D. A. & Krasnitz, A. CNprep:Copy
1047 Number Event Detection. (2020).
1048 89. Li, H. & Durbin, R. Fast and accurate short read alignment with Burrows–Wheeler
1049 transform. *Bioinformatics* **25**, 1754–1760 (2009).
1050 90. Li, H. *et al.* The Sequence Alignment/Map format and SAMtools. *Bioinforma. Oxf. Engl.*
1051 **25**, 2078–2079 (2009).
1052 91. Barnett, D. W., Garrison, E. K., Quinlan, A. R., Strömberg, M. P. & Marth, G. T.
1053 BamTools: a C++ API and toolkit for analyzing and managing BAM files. *Bioinformatics* **27**,
1054 1691–1692 (2011).
1055 92. Koboldt, D. C. *et al.* VarScan 2: somatic mutation and copy number alteration discovery
1056 in cancer by exome sequencing. *Genome Res.* **22**, 568–576 (2012).
1057 93. Wang, K., Li, M. & Hakonarson, H. ANNOVAR: functional annotation of genetic
1058 variants from high-throughput sequencing data. *Nucleic Acids Res.* **38**, e164 (2010).
1059 94. Landrum, M. J. *et al.* ClinVar: improving access to variant interpretations and supporting
1060 evidence. *Nucleic Acids Res.* **46**, D1062–D1067 (2018).
1061 95. Mayakonda, A., Lin, D.-C., Assenov, Y., Plass, C. & Koeffler, H. P. Maftools: efficient
1062 and comprehensive analysis of somatic variants in cancer. *Genome Res.* **28**, 1747–1756
1063 (2018).
1064 96. Wang, Z. *et al.* SMASH, a fragmentation and sequencing method for genomic copy
1065 number analysis. *Genome Res.* **26**, 844–851 (2016).

bioRxiv preprint doi: https://doi.org/10.64898/2026.04.21.720027; this version posted April 24, 2026. The copyright holder for this preprint (which was not certified by peer review) is the author/funder, who has granted bioRxiv a license to display the preprint in perpetuity. It is made available under a CC-BY-NC-ND 4.0 International license.

97. Gu, Z., Eils, R. & Schlesner, M. Complex heatmaps reveal patterns and correlations in multidimensional genomic data. *Bioinforma. Oxf. Engl.* **32**, 2847–2849 (2016).

98. Belleau, P., Deschênes, A., Beyaz, S., Tuveson, D. A. & Krasnitz, A. CNVMetrics package: Quantifying similarity between copy number profiles.

99. Deschênes, A., Belleau, P., Tuveson, D. A. & Krasnitz, A. Quantifying similarity between copy number profiles with CNVMetrics package.

100. Zheng, G. X. Y. *et al.* Massively parallel digital transcriptional profiling of single cells. *Nat. Commun.* **8**, 14049 (2017).

101. Frankish, A. *et al.* GENCODE reference annotation for the human and mouse genomes. *Nucleic Acids Res.* **47**, D766–D773 (2019).

102. Edwards, N. *et al.* SCExecute: custom cell barcode-stratified analyses of scRNA-seq data. *Bioinformatics* **39**, btac768 (2023).

103. Belleau, P., Deschênes, A., Chambwe, N., Tuveson, D. A. & Krasnitz, A. Genetic Ancestry Inference from Cancer-Derived Molecular Data across Genomic and Transcriptomic Platforms. *Cancer Res.* **83**, 49–58 (2023).

104. Shen, R. & Seshan, V. E. FACETS: allele-specific copy number and clonal heterogeneity analysis tool for high-throughput DNA sequencing. *Nucleic Acids Res.* **44**, e131 (2016).

105. Wang, W. *et al.* Single-cell transcriptomic atlas of the human endometrium during the menstrual cycle. *Nat. Med.* **26**, 1644–1653 (2020).

106. Martinez-de-Morentin, X. *et al.* LIBRA: an adaptative integrative tool for paired single-cell multi-omics data. *Quant. Biol. Beijing China* **11**, 246–259 (2023).

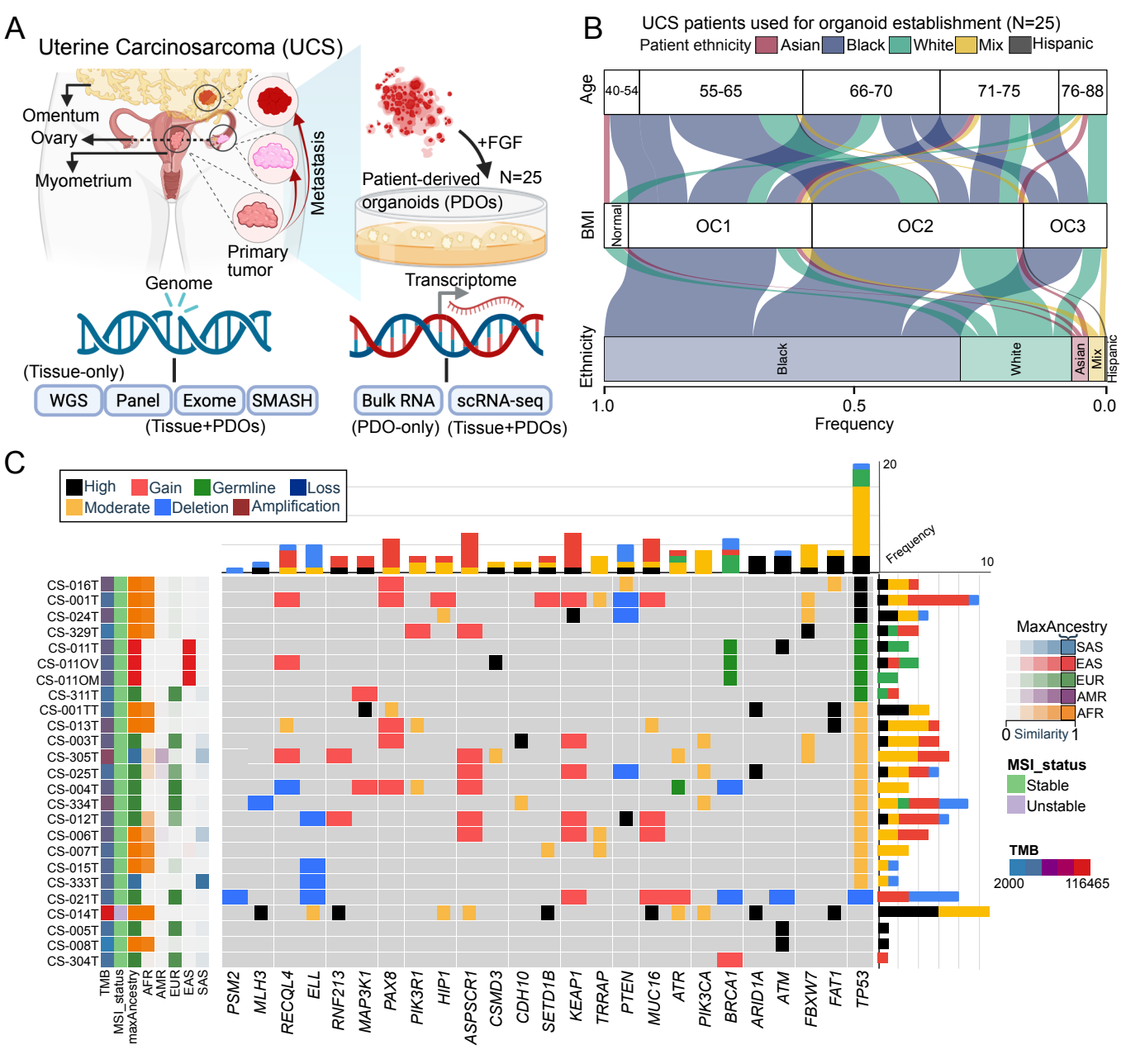
A
Uterine Carcinosarcoma (UCS)
Omentum
Ovary
Myometrium
Primary tumor
Metastasis
+FGF
N=25
Patient-derived organoids (PDOs)
Genome
Transcriptome
(Tissue-only)
WGS
Panel
Exome
SMASH
(Tissue+PDOs)
Bulk RNA
scRNA-seq
(PDO-only)
(Tissue+PDOs)
B
UCS patients used for organoid establishment (N=25)
Patient ethnicity
Asian
Black
White
Mix
Hispanic
Age
40-54
55-65
66-70
71-75
76-88
BMI
Normal
OC1
OC2
OC3
Ethnicity
Black
White
Asian
Mix
Hispanic
1.0
0.5
0.0
Frequency
C
High
Gain
Germline
Loss
Moderate
Deletion
Amplification
20
10
Frequency
CS-016T
CS-001T
CS-024T
CS-329T
CS-011T
CS-011OV
CS-011OM
CS-311T
CS-001TT
CS-013T
CS-003T
CS-305T
CS-025T
CS-004T
CS-334T
CS-012T
CS-006T
CS-007T
CS-015T
CS-333T
CS-021T
CS-014T
CS-005T
CS-008T
CS-304T
TMB
MSI_status
maxAncestry
AFR
AMR
EUR
EAS
SAS
PSM2
MLH3
RECQL4
ELL
RNF213
MAP3K1
PAX8
PIK3R1
HIP1
ASPSCR1
CSMD3
CDH10
SETD1B
KEAP1
TRRAP
PTEN
MUC16
ATR
PIK3CA
BRCA1
ARID1A
ATM
FBXW7
FAT1
TP53
MaxAncestry
SAS
EAS
EUR
AMR
AFR
0 Similarity 1
MSI_status
Stable
Unstable
TMB
2000
116465

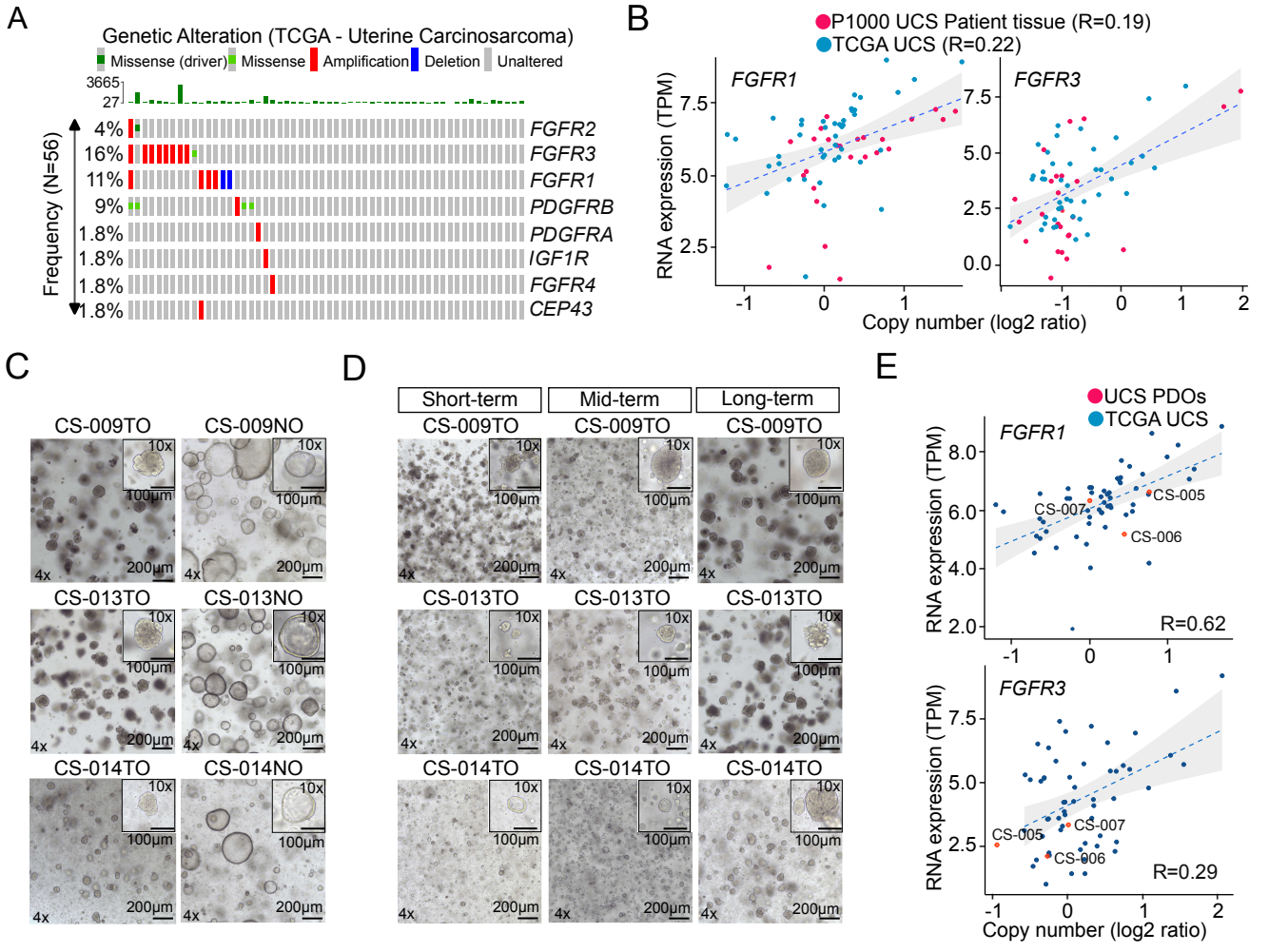
A
Genetic Alteration (TCGA - Uterine Carcinosarcoma)
Missense (driver)
Missense
Amplification
Deletion
Unaltered
3665
27
Frequency (N=56)
4%
16%
11%
9%
1.8%
1.8%
1.8%
1.8%
FGFR2
FGFR3
FGFR1
PDGFRB
PDGFRA
IGF1R
FGFR4
CEP43
B
P1000 UCS Patient tissue (R=0.19)
TCGA UCS (R=0.22)
FGFR1
FGFR3
RNA expression (TPM)
Copy number (log2 ratio)
C
CS-009TO
CS-009NO
CS-013TO
CS-013NO
CS-014TO
CS-014NO
10x
100μm
4x
200μm
D
Short-term
Mid-term
Long-term
CS-009TO
CS-013TO
CS-014TO
E
UCS PDOs
TCGA UCS
FGFR1
FGFR3
CS-005
CS-006
CS-007
R=0.62
R=0.29
RNA expression (TPM)
Copy number (log2 ratio)

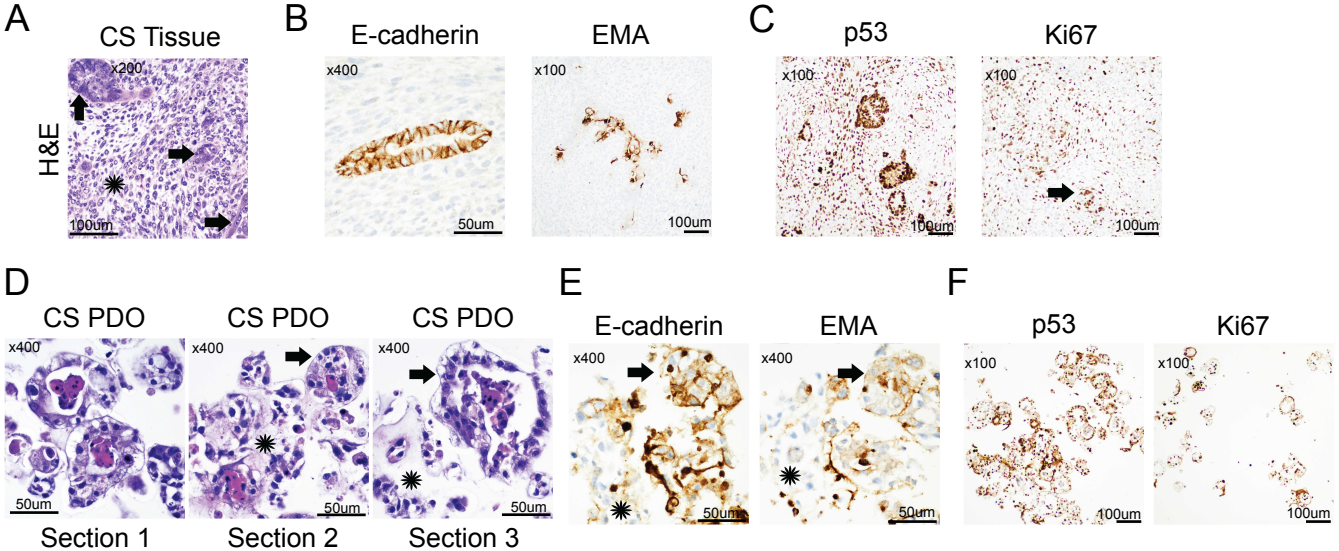
A
CS Tissue
H&E
x200
100um
B
E-cadherin
x400
50um
EMA
x100
100um
C
p53
x100
100um
Ki67
x100
100um
D
CS PDO
CS PDO
CS PDO
x400
x400
x400
50um
50um
50um
Section 1
Section 2
Section 3
E
E-cadherin
x400
50um
EMA
x400
50um
F
p53
x100
100um
Ki67
x100
100um

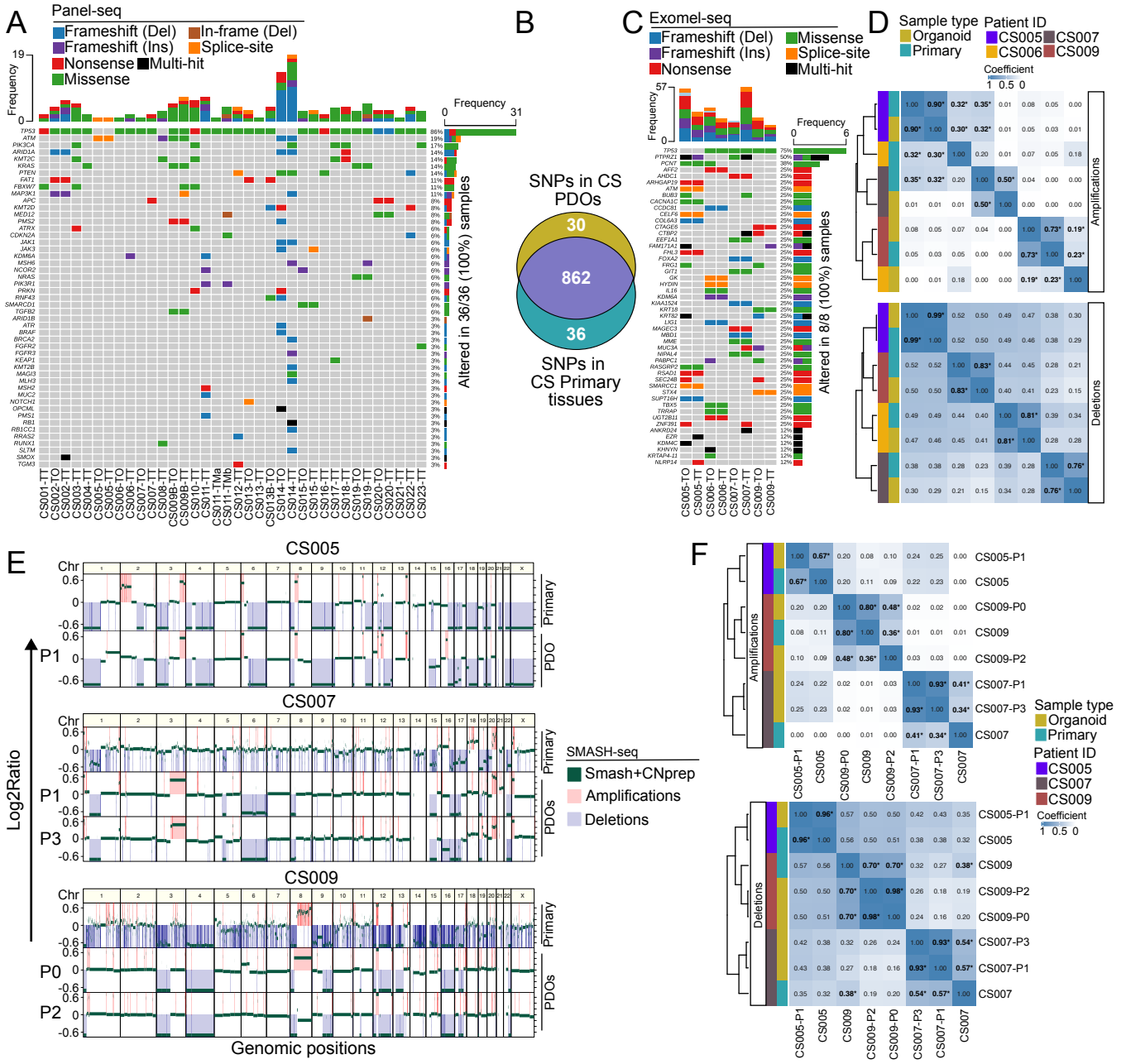
A
Panel-seq
Frameshift (Del)
Frameshift (Ins)
Nonsense
Missense
In-frame (Del)
Splice-site
Multi-hit
Frequency
Altered in 36/36 (100%) samples
B
SNPs in CS PDOs
30
862
36
SNPs in CS Primary tissues
C
Exomel-seq
Frameshift (Del)
Frameshift (Ins)
Nonsense
Missense
Splice-site
Multi-hit
Altered in 8/8 (100%) samples
D
Sample type
Organoid
Primary
Patient ID
CS005
CS006
CS007
CS009
Coefficient
Amplifications
Deletions
E
CS005
CS007
CS009
Chr
Primary
PDO
PDOs
P1
P3
P0
P2
Log2Ratio
SMASH-seq
Smash+CNprep
Amplifications
Deletions
Genomic positions
F
Amplifications
Deletions
Sample type
Organoid
Primary
Patient ID
CS005
CS007
CS009
Coefficient

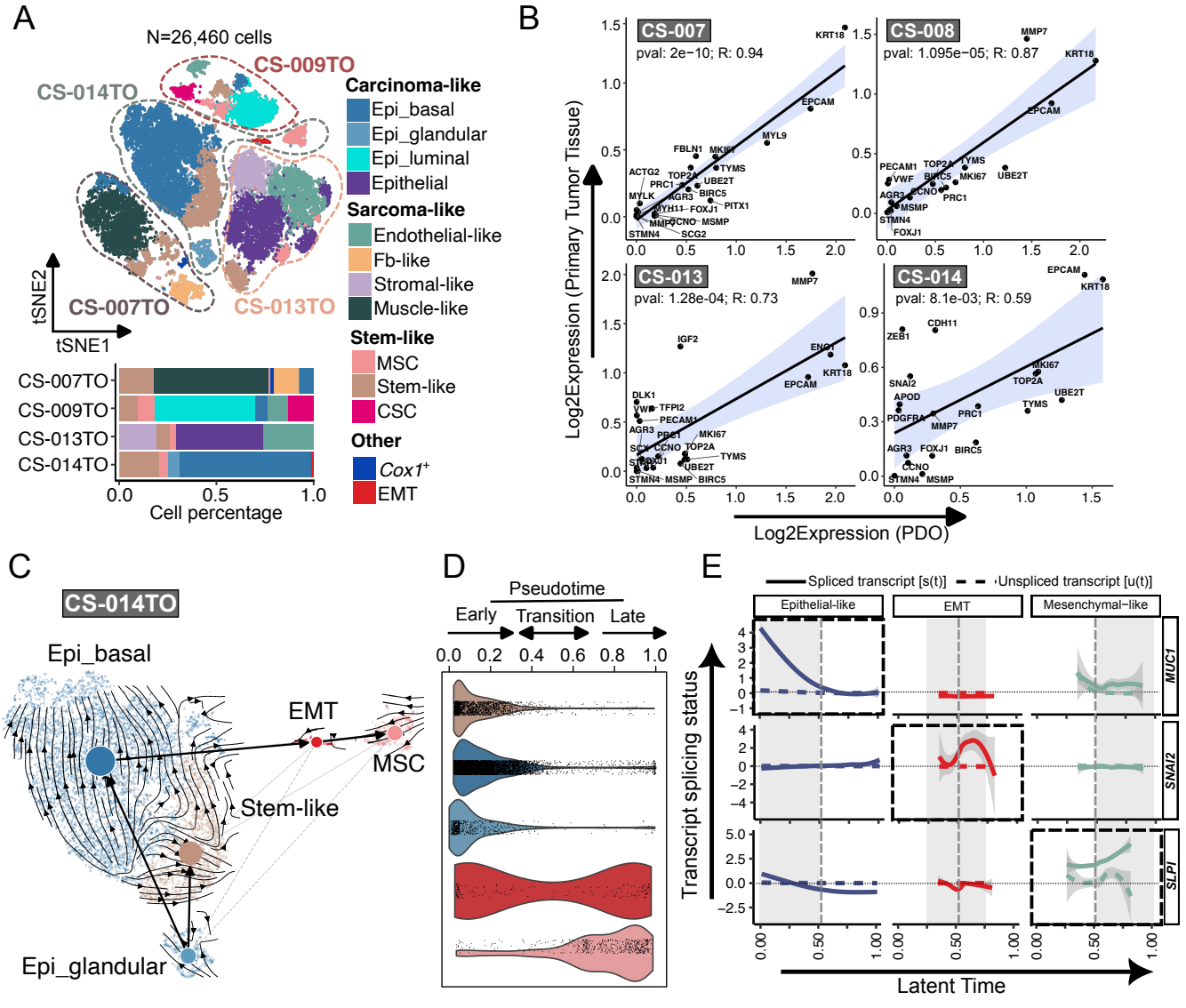
A
N=26,460 cells
CS-009TO
CS-014TO
CS-007TO
CS-013TO
tSNE2
tSNE1
Carcinoma-like
Epi_basal
Epi_glandular
Epi_luminal
Epithelial
Sarcoma-like
Endothelial-like
Fb-like
Stromal-like
Muscle-like
Stem-like
MSC
Stem-like
CSC
Other
Cox1+
EMT
CS-007TO
CS-009TO
CS-013TO
CS-014TO
0.0
0.5
1.0
Cell percentage
B
CS-007
pval: 2e−10; R: 0.94
CS-008
pval: 1.095e−05; R: 0.87
CS-013
pval: 1.28e-04; R: 0.73
CS-014
pval: 8.1e-03; R: 0.59
Log2Expression (Primary Tumor Tissue)
Log2Expression (PDO)
C
CS-014TO
Epi_basal
EMT
MSC
Stem-like
Epi_glandular
D
Pseudotime
Early
Transition
Late
0.0 0.2 0.4 0.6 0.8 1.0
E
Spliced transcript [s(t)]
Unspliced transcript [u(t)]
Epithelial-like
EMT
Mesenchymal−like
MUC1
SNAI2
SLPI
Transcript splicing status
Latent Time

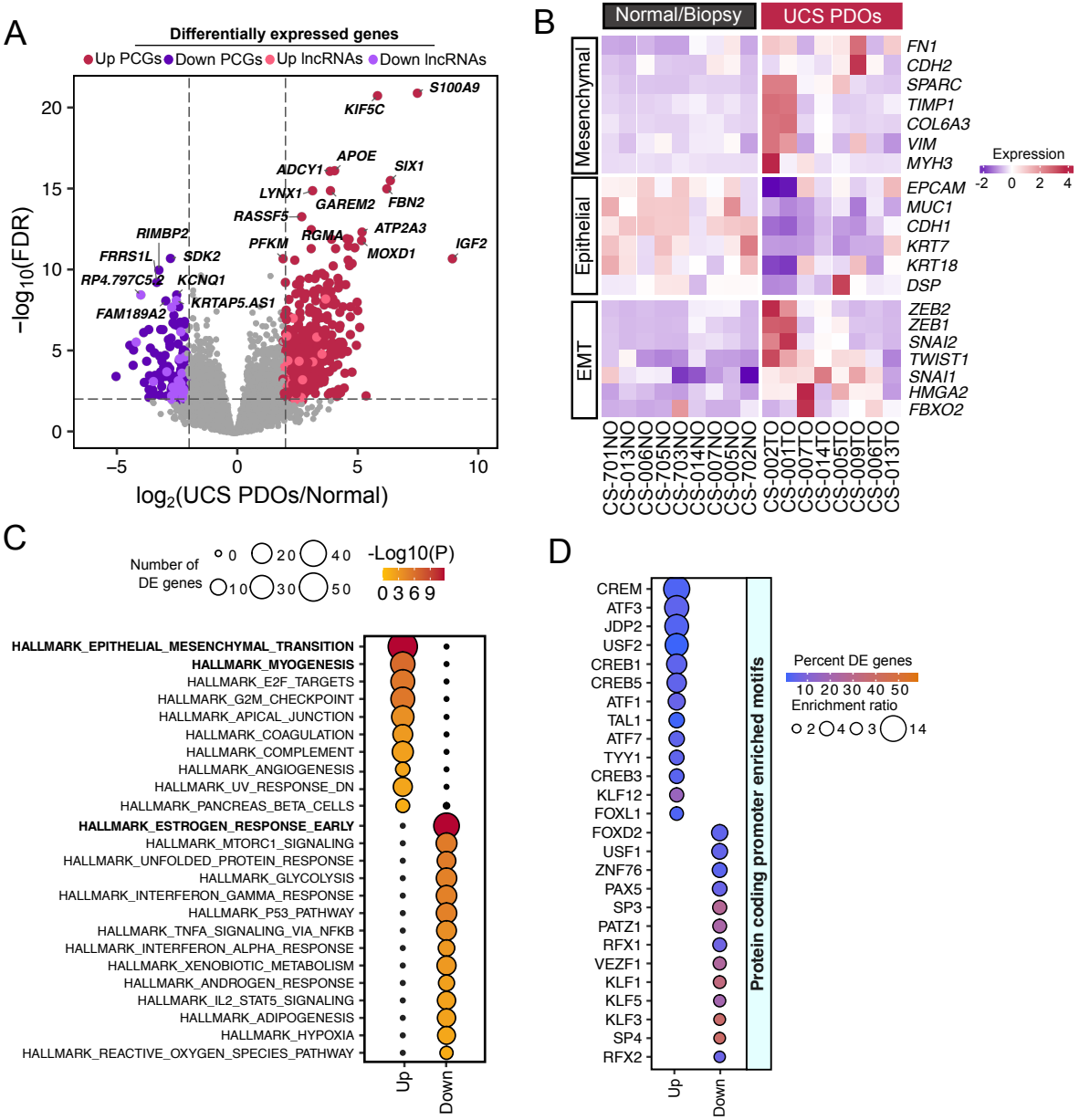
A
Differentially expressed genes
Up PCGs
Down PCGs
Up lncRNAs
Down lncRNAs
S100A9
KIF5C
APOE
ADCY1
SIX1
LYNX1
GAREM2
FBN2
RASSF5
ATP2A3
RIMBP2
RGMA
PFKM
IGF2
FRRS1L
SDK2
MOXD1
RP4.797C5.2
KCNQ1
KRTAP5.AS1
FAM189A2
−log10(FDR)
log2(UCS PDOs/Normal)
B
Normal/Biopsy
UCS PDOs
Mesenchymal
Epithelial
EMT
FN1
CDH2
SPARC
TIMP1
COL6A3
VIM
MYH3
EPCAM
MUC1
CDH1
KRT7
KRT18
DSP
ZEB2
ZEB1
SNAI2
TWIST1
SNAI1
HMGA2
FBXO2
Expression
CS-701NO
CS-013NO
CS-006NO
CS-705NO
CS-703NO
CS-014NO
CS-005NO
CS-702NO
CS-002TO
CS-001TO
CS-007TO
CS-014TO
CS-005TO
CS-009TO
CS-006TO
CS-013TO
C
Number of DE genes
-Log10(P)
HALLMARK_EPITHELIAL_MESENCHYMAL_TRANSITION
HALLMARK_MYOGENESIS
HALLMARK_E2F_TARGETS
HALLMARK_G2M_CHECKPOINT
HALLMARK_APICAL_JUNCTION
HALLMARK_COAGULATION
HALLMARK_COMPLEMENT
HALLMARK_ANGIOGENESIS
HALLMARK_UV_RESPONSE_DN
HALLMARK_PANCREAS_BETA_CELLS
HALLMARK_ESTROGEN_RESPONSE_EARLY
HALLMARK_MTORC1_SIGNALING
HALLMARK_UNFOLDED_PROTEIN_RESPONSE
HALLMARK_GLYCOLYSIS
HALLMARK_INTERFERON_GAMMA_RESPONSE
HALLMARK_P53_PATHWAY
HALLMARK_TNFA_SIGNALING_VIA_NFKB
HALLMARK_INTERFERON_ALPHA_RESPONSE
HALLMARK_XENOBIOTIC_METABOLISM
HALLMARK_ANDROGEN_RESPONSE
HALLMARK_IL2_STAT5_SIGNALING
HALLMARK_ADIPOGENESIS
HALLMARK_HYPOXIA
HALLMARK_REACTIVE_OXYGEN_SPECIES_PATHWAY
Up
Down
D
CREM
ATF3
JDP2
USF2
CREB1
CREB5
ATF1
TAL1
ATF7
TYY1
CREB3
KLF12
FOXL1
FOXD2
USF1
ZNF76
PAX5
SP3
PATZ1
RFX1
VEZF1
KLF1
KLF5
KLF3
SP4
RFX2
Protein coding promoter enriched motifs
Percent DE genes
Enrichment ratio
Up
Down

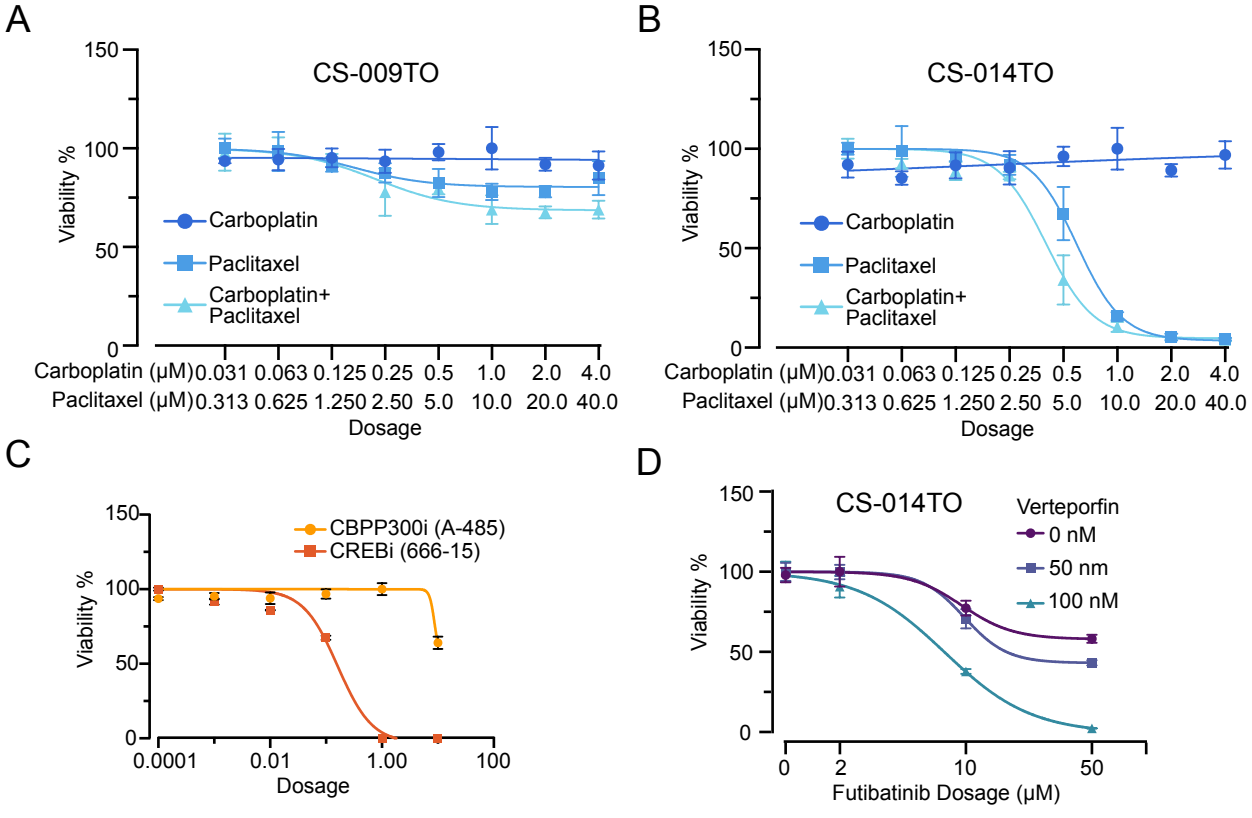
A
CS-009TO
Viability %
150
100
50
0
Carboplatin
Paclitaxel
Carboplatin+
Paclitaxel
Carboplatin (μM) 0.031 0.063 0.125 0.25 0.5 1.0 2.0 4.0
Paclitaxel (μM) 0.313 0.625 1.250 2.50 5.0 10.0 20.0 40.0
Dosage
B
CS-014TO
Viability %
150
100
50
0
Carboplatin
Paclitaxel
Carboplatin+
Paclitaxel
Carboplatin (μM) 0.031 0.063 0.125 0.25 0.5 1.0 2.0 4.0
Paclitaxel (μM) 0.313 0.625 1.250 2.50 5.0 10.0 20.0 40.0
Dosage
C
CBPP300i (A-485)
CREBi (666-15)
Viability %
150
100
50
0
0.0001
0.01
1.00
100
Dosage
D
CS-014TO
Verteporfin
0 nM
50 nm
100 nM
Viability %
150
100
50
0
0
2
10
50
Futibatinib Dosage (μM)

bioRxiv preprint doi: https://doi.org/10.64898/2026.04.21.720027; this version posted April 24, 2026. The copyright holder for this preprint (which was not certified by peer review) is the author/funder, who has granted bioRxiv a license to display the preprint in perpetuity. It is made available under a CC-BY-NC-ND 4.0 International license.

Figure 1: Genomic profiling defines an ancestrally enriched uterine carcinosarcoma cohort.
(**A**) Schematic overview of sample collection and experimental workflow. Twenty-five tumor specimens from patients with uterine carcinosarcoma (UCS) were collected (n = 23 primary tumors; n = 2 metastases), with matched normal tissue when available, for the establishment of patient-derived organoids (PDOs). These established UCS PDOs along with the primary tissues were sequenced using multiple genomic panels such as targeted Panel-seq (n = 36), Whole exome-seq (n = 8), and genome-wide copy-number profiling by SMASH-seq (n = 6). Whole genome sequencing (WGS) was only generated for primary tissues (n = 25). Single cell transcriptome was generated for both UCS PDOs and the primary tissues (n = 4). Bulk RNA-seq was only performed for PDOs (n = 17).
(**B**) Alluvial plots show the overall distribution of UCS patients (n = 13) from which UCS PDOs are established in this study. This includes self-reported ethnicity (African American (AFR) n = 12, Asian (AS) n = 3, European/White (EUR) n = 6, mixed ethnicity (MIX) n = 3, and Hispanic n=1), body mass index (BMI), and age groups. The BMI groups are classified based on their BMI indices such as Normal >= 18.5 & < 25; Obese class 1 (OC1) >= 25 & < 30; Obese class 2 (OC2) >= 30 & < 40; Obese class 3 (OC3) >= 40.
(**C**) Genomic landscape of the UCS cohort based on WGS. Heatmap displays recurrent somatic alterations across 25 UCS tissue specimens and tumor mutational burden (TMB). Microsatellite instability (MSI) status was assessed using MANTIS. Ancestry inference was performed using ADMIXTURE analysis and was concordant with self-reported ethnicity. AFR: African American; AS: Asian; EUR: European/White; EAS: East Asian; SAS: South Asian.

bioRxiv preprint doi: https://doi.org/10.64898/2026.04.21.720027; this version posted April 24, 2026. The copyright holder for this preprint (which was not certified by peer review) is the author/funder, who has granted bioRxiv a license to display the preprint in perpetuity. It is made available under a CC-BY-NC-ND 4.0 International license.

Figure 2: Recurrent FGFR alterations support FGF-dependent establishment and genomic fidelity of UCS PDOs.

(**A**) Frequency and spectrum of recurrent genetic alterations in receptor tyrosine kinase and growth factor signaling genes in UCS from the TCGA cohort (n = 56). Alterations include non-synonymous somatic mutations and high-level copy-number gains or deletions. Thresholds to assign a significant alteration were set to p-value < 0.001 for deletions and p-value > 0.999 for amplifications.

(**B**) Copy-number-expression correlation analysis for *FGFR1* and *FGFR3* in primary UCS tumors from our cohort (red; n = 25) compared with TCGA-UCS samples (blue; n = 56). Log2 copy-number ratios derived from whole-genome sequencing were plotted against transcript abundance (TPM) from bulk RNA sequencing. Correlation coefficients were calculated using Spearman method.

(**C**) Representative brightfield images of matched normal endometrial and UCS PDOs for donors CS-009, CS-013, and CS-014. Scale bars: 4X: 200 µm; 10X: 100 µm.

(**D**) Representative brightfield images of the long-term expansion of representative UCS PDO lines (CS-009, CS-013, and CS-014) maintained in culture for up to 28 months. Images show organoid morphology at indicated time points. Short-term:0.5-1.5 months; Mid-term: 5-8 months; Long-term: 18-28 months. Scale bars: 4X: 200 µm; 10X: 100 µm.

(**E**) Copy-number-expression correlation for *FGFR1* and *FGFR3* in matched UCS PDOs (red, n = 3) compared with TCGA-UCS samples (blue; n = 56). Log2 copy-number ratios were derived from whole-exome sequencing and plotted against bulk RNA expression (TPM). Correlation was assessed using Spearman method.

bioRxiv preprint doi: https://doi.org/10.64898/2026.04.21.720027; this version posted April 24, 2026. The copyright holder for this preprint (which was not certified by peer review) is the author/funder, who has granted bioRxiv a license to display the preprint in perpetuity. It is made available under a CC-BY-NC-ND 4.0 International license.

Figure 3: UCS PDOs retain the histologic and immunophenotypic features of primary tumors.

(**A**) Representative images of hematoxilin & eosin (H&E) staining of primary UCS tumor tissue section showing malignant epithelial glands (arrows) surrounded by highly atypical stroma (asterisk), representing malignant mesodermal differentiation of the tumor. Original magnification 400X. Scale bar: 100 µm.

(**B**) Representative immunostaining of UCS PDOs for E-cadherin and epithelial membrane antigen (EMA). The epithelial organoids are positive for E-cadherin, while the surrounding neoplastic stroma shows negative staining. Original magnification 400X. Scale bar: 50 µm. Similar, EMA staining shows that epithelial elements are multifocally positive, while the malignant stroma is negative. Original magnification 100X. Scale bar: 100 µm.

(**C**) Representative immunostaining of UCS PDOs for p53 shows diffusely positive staining, including the neoplastic stroma in the uterine tumor. Scale bar: 100 µm. Representative immunostaining of UCS PDOs for Ki67 shows markedly increased proliferative index. Both the neoplastic glands (like the one marked by the arrow) and the surrounding neoplastic stroma are diffusely positive. Original magnification 100X. Scale bar: 100 µm.

(**D**) Representative H&E UCS PDO sections (S1, S2, and S3), consisting of the malignant epithelial elements of the tumor, show high-grade nuclear atypia and central necrosis (S1). Other areas show PDOs (arrow) with adjacent neoplastic cells not arranged in epithelial-like structures (star) (S2). In addition, an area suggestive of extracellular matrix formation is seen in (S3). Original magnification 50X. Scale bar 100 µm.

(**E**) Representative immunostaining of UCS PDOs for E-cadherin. The epithelial PDOs (arrow) show positive staining, while the adjacent disorganized neoplastic cells are negative (star). Scale bar: 50 µm. Representative immunostaining of the organoids for EMA shows that the epithelial elements (arrow) are multifocally positive, while the adjacent disorganized tumor cells are negative (star). Original magnification 400X. Scale bar: 50 µm.

(**F**) Representative immunostaining of UCS PDOs for p53 shows diffusely positive signals, including the neoplastic stroma. Scale bar: 100µm. Representative immunostaining of Ki67 shows increased signal. Both the neoplastic glands (arrow) and the surrounding neoplastic stroma are diffusely positive. Original magnification 100X. Scale bar: 100 µm.

bioRxiv preprint doi: https://doi.org/10.64898/2026.04.21.720027; this version posted April 24, 2026. The copyright holder for this preprint (which was not certified by peer review) is the author/funder, who has granted bioRxiv a license to display the preprint in perpetuity. It is made available under a CC-BY-NC-ND 4.0 International license.

Figure 4: Preservation of mutational and copy-number landscapes in UCS PDOs.
(**A**) Targeted panel-seq of 49 cancer-associated genes in UCS tumors (n = 25; 23 primary tumors, 2 metastases) and matched PDOs (n = 10 matched pairs). Oncoplot displays distribution of somatic mutations across samples.
(**B**) Venn diagram besides oncoplot illustrates the overlap of detected single nucleotide polymorphisms (SNPs) within the targeted regions between primary tumors and matched PDOs, comprising 862 shared variants, 36 primary-specific SNPs, and 30 PDO-specific SNPs.
(**C**) Whole-exome sequencing (WES) oncoplot shows comparison of somatic mutational profiles between matched tumor-PDO pairs (n = 4 matched donors).
(**D**) Heatmaps showing the Sørensen similarity indexes between CS tumors (TT) and PDOs (TO) exome profiles of chromosomal aberrations (Deletion and Amplification). In the heatmap value of 0 indicates no similarity, while 1 indicates exact similarity. * indicates the similarity index is significant with p-value < 0.05 calculated using simulations.
(**E**) Genome-wide copy-number profiles generated by SMASH sequencing for primary tumors and matched PDOs across multiple passages. Log2 copy-number ratios are plotted across chromosomes. Regions with significant amplification and deletion events are respectively colored in pink and light blue.
(**F**) Heatmaps showing correlation in amplification and deletion profiles between matched tumor-PDO pairs was performed using Sørensen correlation test. In the heatmap value of 0 indicates no similarity, while 1 indicates exact similarity. The * indicates the similarity index is significant with p-value < 0.05 calculated using simulations.

bioRxiv preprint doi: https://doi.org/10.64898/2026.04.21.720027; this version posted April 24, 2026. The copyright holder for this preprint (which was not certified by peer review) is the author/funder, who has granted bioRxiv a license to display the preprint in perpetuity. It is made available under a CC-BY-NC-ND 4.0 International license.

Figure 5: UCS PDOs preserve dynamic epithelial-mesenchymal transitions.
(**A**) t-SNE representation of single-cell RNA sequencing (scRNA-seq) data (N= 51,784 cells) from four independent UCS PDO lines (CS-007TO, CS-009TO, CS-013TO, CS-014TO). Cells are colored by annotated cell subtype, including carcinoma-associated (epithelial basal, glandular, luminal, and epithelial populations), sarcoma-associated (endothelial-like, fibroblast-like (Fb-like), stromal-like, and muscle-like), stem-associated (mesenchymal stem cells (MSCs), stem-like, cancer stem cells (CSCs)), as well as other (*Cox1*$^{+}$, EMT). Bar plot (below) shows proportional representation of each cell type per donor.
(**B**) Correlation analysis of total gene expression signatures between matched primary tumors and PDOs. Each point represents a UCS donor. X-axis consists of log2 transformed expression in UCS PDOs and Y-axis consists of log2 transformed expression in primary UCS tumors. The correlation and p-values values are calculated using Pearson correlation coefficient.
(**C**) RNA velocity analysis of representative PDO CS-014TO, showing directional transcriptional flow from epithelial basal and glandular populations toward EMT and stem- and MSC-like states. Velocity vectors were computed using scVelo based on spliced and unspliced transcript counts.
(**D**) Pseudotime of transcripts from individual cells of PDO CS-014TO is inferred using scVelo, indicating early epithelial, transitional, and late mesenchymal states along a continuous trajectory. Pseudotime represents an unobserved, relative distance along a trajectory or differentiation time from one point to another (here, 0 to 1), inferred via transcriptomic similarity in individual cells.
(**E**) Latent time derived from RNA velocity of PDO CS-014TO, illustrating dynamic progression across lineage states. Representative genes (*MUC1*, *SNAI2*, *SLPI*) are plotted across latent time to demonstrate sequential activation of epithelial, EMT, and mesenchymal programs.

bioRxiv preprint doi: https://doi.org/10.64898/2026.04.21.720027; this version posted April 24, 2026. The copyright holder for this preprint (which was not certified by peer review) is the author/funder, who has granted bioRxiv a license to display the preprint in perpetuity. It is made available under a CC-BY-NC-ND 4.0 International license.

Figure 6: Transcriptional reprogramming in UCS PDOs reveals mesenchymal activation and CREB-associated motifs

(**A**) Volcano plot of differential gene expression between UCS PDOs (n = 8) and normal endometrial biopsy-derived organoids (NO; n = 9). Significantly deregulated genes (FDR < 0.05; log2 fold change≥ 1) are highlighted in red (upregulated) and blue (downregulated). Selected top upregulated and downregulated protein-coding genes and long non-coding RNAs (lncRNAs) are indicated.

(**B**) Heatmap of lineage-associated gene signatures across UCS and normal PDOs, showing downregulation of epithelial markers and upregulation of mesenchymal and epithelial EMT-associated genes in UCS PDOs. Gene expression values are shown as Z-score-scaled log2-transformed counts.

(**C**) Hallmark pathway enrichment analysis of differentially expressed genes comparing UCS and normal PDOs. Significance of the pathways were determined by p-values obtained using GeneSCF tool. Size of the dots represent number of differentially expressed genes in UCS involved in corresponding pathways and the color gradient shows -log10 transformed p-values, -log10(p-value). Higher the -log10(p-value) means the pathways are significantly enriched.

(**D**) Promoter motif enrichment analysis of upregulated and downregulated protein coding genes in UCS PDOs relative to NO controls. Motif enrichment was assessed using SEA (Simple Enrichment Analysis) from MEME Suite, revealing significant enrichment of CREB-family transcription factor binding motifs (CREB1, CREB3, CREB5, CREM). Enrichment ratio was calculated using ratio of true positives and false positive sequences determined by SEA. The color gradient represents percentage of differentially expressed genes in UCS regulated by corresponding transcription factors.

bioRxiv preprint doi: https://doi.org/10.64898/2026.04.21.720027; this version posted April 24, 2026. The copyright holder for this preprint (which was not certified by peer review) is the author/funder, who has granted bioRxiv a license to display the preprint in perpetuity. It is made available under a CC-BY-NC-ND 4.0 International license.

Figure 7: UCS PDOs serve as model to investigate in drug-response effects.
(**A**) Dose-response curves of UCS PDO CS-009TO treated with Carboplatin (0.03125-4 µM), Paclitaxel (0.3125 µM-40 µM), and a combination of both. PDOs were treated for 6 days, and viability was quantified using the CellTiter-Glo 3D luminescent assay. Data is normalized to vehicle control and presented as mean ± SD from n = 4 technical replicates.
(**B**) Dose-response curves of UCS PDO CS-014TO treated with Carboplatin (0.03125-4 µM), Paclitaxel (0.3125 µM-40 µM), and a combination of both. PDOs were treated for 6 days, and viability was quantified using the CellTiter-Glo 3D luminescent assay. Data is normalized to vehicle control and presented as mean ± SD from n = 4 technical replicates.
(**C**) Dose-response curves of UCS PDO CS-014TO treated with CBPP300i (A-485, 1 nM-1000 nM) and CREBi (666-15, 1 nM-1000 nM). PDOs were treated for 6 days, and viability was quantified using the CellTiter-Glo 3D luminescent assay. Data is normalized to vehicle control and is shown as mean ± SD, with n = 8 (0 nM control) and n = 4 (treatment condition).
(**E**) Dose-response curves of the UCS PDO line CS-014TO treated with Verteporfin (50-100 nM), Futibatinib (2-50 µM), or their combination. PDOs were treated for 6 days, and cell viability was assessed using the CellTiter-Glo 3D luminescence assay. Data is normalized to vehicle control and presented as mean ± SD, with n = 4 technical replicates for each treatment condition.